Magnetic Oxide Heterostructures

Anand Bhattacharya[1] and Steven J. May[2]

[1]Materials Science Division and Center for Nanoscale Materials, Argonne National Laboratory, Argonne, Illinois 60439; email: anand@anl.gov

[2]Department of Materials Science and Engineering, Drexel University, Philadelphia, Pennsylvania 19104; email: smay@coe.drexel.edu

Annu. Rev. Mater. Res. 2014. 44:65–90

First published online as a Review in Advance on February 24, 2014

The *Annual Review of Materials Research* is online at matsci.annualreviews.org

This article's doi:
10.1146/annurev-matsci-070813-113447

Keywords

magnetism, complex oxides, epitaxial heterostructures, interfacial phenomena, perovskites

Abstract

Complex transition metal oxides have played a central role in the study of magnetic materials, serving as model systems for explorations of fundamental exchange interactions and the relationships between structural, electronic, and magnetic responses. Enabled by advances in epitaxial synthesis techniques, abrupt heterointerfaces and superlattices have emerged as a powerful platform for engineering novel magnetic behavior in oxides. Following a brief introduction to the dominant exchange mechanisms in metal oxides, we review the general means by which interfacial magnetism can be tailored in ABO_3 perovskites, including interfacial charge transfer, epitaxial strain and structural coupling, orbital polarizations and reconstructions, and tailoring exchange interactions via cation ordering. Recent examples are provided to illustrate how these strategies have been employed at isolated interfaces and in short-period superlattices. We conclude by briefly discussing underexplored and emerging research directions in the field.

1. INTRODUCTION

Complex oxides incorporating 3*d* transition metals, in particular ABO_3 perovskites and AB_2O_4 spinels, have been fertile ground for the discovery and application of many novel forms of magnetism (1). Such developments are due to (*a*) the nature of the electronic states that arise when 3*d* transition metals hybridize with oxygen and (*b*) the bonding geometries in these structures (2). In recent years, creating atomically sharp interfaces in epitaxial complex oxide heterostructures has become possible (3). The result is new opportunities to realize model systems in which exchange interactions can be tailored on an atomic length scale, yielding novel magnetic properties and perhaps even new applications. In addition to the usual exchange interactions found in complex oxides, interfaces enable new effects that include charge transfer, structural coupling, and orbital reconstructions. With advances in synthesis and modeling, this area of research is ripe for explorations to advance our fundamental understanding.

In this review, we focus on ABO_3 perovskite heterostructures. In the first part, we summarize the structural and electronic properties of ABO_3 perovskites and the magnetic interactions that arise at interfaces. We follow with several examples showing how novel magnetic behavior has been realized in this class of materials. We focus on the fundamental mechanisms by which the exchange interactions, and resultant magnetic properties such as spin structure and ordering temperatures, are altered at interfaces. We omit more applied topics such as oxide spintronics (see Reference 4) and areas such as exchange bias and multiferroic heterostructures, about which thorough reviews have already been written (5, 6).

2. STRUCTURE AND MAGNETISM IN PEROVSKITES

We begin with a brief introduction to perovskite structure. In ABO_3 perovskites, the transition metal cation occupies the *B*-site (**Figure 1**), coordinated with six O^{2-} anions in corner-connected BO_6 octahedra. The interstitial *A*-sites are occupied by a cation (e.g., alkaline earth or lanthanide), whose oxidation state determines the electron count on the *B*-site transition metal. Besides the charge state of the *B*-site cation, the geometry of the *B*-O-*B* network plays an important role in magnetic properties. The *B*-O-*B* bonding environment is determined partly by the relative sizes of the *A* and *B* cations. For a perfectly cubic ABO_3 unit cell with 180° *B*-O-*B* bond angles, the *A*-O and *B*-O bond lengths are such that the Goldschmidt tolerance factor (7) $t = r_{A\text{-}O}/(r_{B\text{-}O}\sqrt{2})$ is 1.0. However, for a large number of magnetic oxides, $0.71 < t < 1$, where the constraints of three-dimensional connectivity and optimal coordination between atoms are accommodated by cooperative tilts and rotations of the BO_6 octahedra (8). For relatively small distortions, this situation leads to pseudocubic structures with orthorhombic, tetragonal, or rhombohedral symmetry. The octahedral rotations alter *B*-O-*B* bond angles and, to a lesser extent, bond lengths. Due to multiple competing magnetic interactions, even relatively small distortions can affect the sign and strength of the exchange interactions mediated through these bonds.

In the *3d* perovskites, the outermost electrons on the transition metal nominally occupy *d* orbitals. The bonding states are mostly of 2*p* character (**Figure 1**), whereas the antibonding states are mostly of 3*d* character (with important exceptions!) and have spins that are primarily responsible for the observed magnetization. Due to electrostatic interactions and hybridization of the 3*d* states with the nearest O^{2-}-2*p* orbitals in a cubic crystal field, the fivefold degeneracy of the *3d* manifold is lifted. The eigenstates are no longer spherical harmonics but are linear combinations of these, with an e_g doublet ($d_{x^2-y^2}$, $d_{3z^2-r^2}$) and a t_{2g} triplet (d_{xy}, d_{yz}, d_{xz}) separated by the crystal field splitting, $\Delta_{CF} \sim 1$–2 eV (**Figure 1**). Due to the loss of degeneracy, the orbital

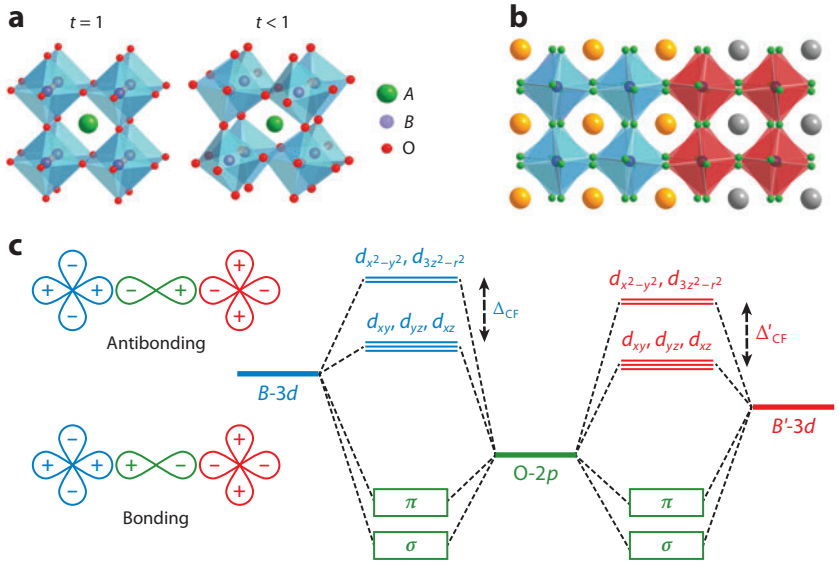

Figure 1

(*a*) Structure for an ABO_3 perovskite, shown with an ideal cubic structure ($t = 1$) and with octahedral tilts ($t < 1$). (*b*) An $ABO_3/A'B'O_3$ interface. (*c*) The electronic configuration at a *B*-O-*B*′ bond at a perovskite interface. The crystal field splitting, Δ_{CF} and Δ'_{CF}, is shown for the *B* and *B*′ cations at the interface.

angular momentum of the 3*d* states is partly quenched. The degeneracy in the e_g and t_{2g} manifolds can be lifted further by structural distortions (e.g., Jahn-Teller effects) (8). The degeneracy in the t_{2g} manifold can also be removed by spin-orbit coupling, although this is not true for the e_g states (12). For the 3*d* oxides considered here, spin-orbit coupling is relatively weak, and we can ignore the orbital component of magnetization to a first approximation. Thus, we assume that the Lande *g* factor is ∼2 and that the magnetic moment is simply $g\mu_B S$, where S is the total spin of the electrons in the 3*d* manifold and $\mu_B = \frac{e\hbar}{2m_e}$ is the Bohr magneton (SI units).

The exchange interaction between electrons is a consequence of Fermi statistics, which prohibits identical electrons (e.g., two spin-up electrons) from occupying the same state, and the *e*-*e* Coulomb repulsion that depends on the spatial part of the electron wave functions. The exchange interaction plays an important role in electronic structure, due to interactions between electrons on the same site as well as on neighboring sites.

For electrons in the 3*d* manifold of a transition metal atom, the intra-atomic interaction favors parallel spin alignment, which minimizes Coulomb repulsion due to Hund's exchange coupling (J_H). For interatomic exchange interactions between localized states, the strength of the interaction is a function of the direct overlap between them. The complex oxides were recognized early on as being different in this regard. In the 3*d* perovskites, the direct overlap between neighboring *B*-site cations is negligible and cannot account for the strength of the exchange interaction (this becomes progressively less true for 4*d* and 5*d* compounds). In fact, the interaction is mediated through the bridging oxygen and directly involves its electrons. Two types of exchange interactions occur in this manner. The first, termed superexchange, involves a virtual transfer of electrons between the transition metal cations. The second, double exchange, involves mediation of magnetic interactions by delocalized carriers. In this section, we briefly describe these interactions and set them in the context of interfaces.

Superexchange

The so-called rules for superexchange are codified in papers by Goodenough (9), Kanamori (10), and Anderson (11) and are thus collectively known as the GKA rules. Khomskii (12) provides an excellent review of these rules, and we refer the reader to this and several other reviews (e.g., Reference 13) for detailed discussions. In our simplified description, we consider a single 3*d* orbital per *B*-site with one electron per orbital. Transfer of electrons between two adjacent *B*-site cations involves two hops, one for each *B*-O bond (see **Figure 2*a***). The effective *d*-*d* hopping integral between orbitals on two identical *B*-site cations is given by $t_{dd} = t_{pd}^2/\Delta$. Here t_{pd} is the *p*-*d* hopping integral, and Δ, the charge transfer gap, is the energy needed for an electron to hop between an O-2*p* and a *B*-3*d* level (more on this below). t_{dd} has important symmetry constraints; for example, two d_{xy} orbitals can connect through a p_x ligand orbital along the *y* direction, but not through p_z or p_y. The combinations of orbitals that participate in exchange are thereby restricted. Let us now consider a lattice of transition metal sites, each initially having *n* electrons in the 3*d* manifold (d^n); all occupied orbitals have exactly one electron. If an electron were to hop between neighboring sites, it would have to pay an energy cost associated with the change in electron count on both the sites involved. This cost, which is mostly due to on-site Coulomb repulsion between electrons, is often referred to as the Mott-Hubbard *U*,

$$U = E(d^{n-1} + d^{n+1}) - E(d^n + d^n). \quad 1.$$

In many 3*d* perovskites, where $U \sim 4$–7 eV and $t_{dd} \sim 0.1$–0.3 eV ($U \gg t_{dd}$), the energy lowered by delocalizing electrons is unable to overcome the Coulomb blockade between sites, and a Mott insulator is obtained for what would be a metallic half-filled band in the noninteracting limit.

However, the electrons can still make virtual hops to neighboring sites, where by second-order perturbation we expect a lowering of energy by an amount given by

$$J = -\frac{2t_{dd}^2}{U}. \quad 2.$$

This virtual hop is allowed by the Pauli principle so long as the virtual state has a spin opposite to that of the electron occupying the orbital. The neighboring sites labeled *i*, *j* are antiferromagnetically coupled with an exchange energy given by $-J\,S_i\,S_j$. The first GKA rule states that exchange interactions between filled 3*d* orbitals on adjacent *B*-site cations are antiferromagnetic (AF); examples include $SrMnO_3$, $LaCrO_3$, and $LaFeO_3$. The factor of 2 in Equation 2 considers both (*a*) virtual hops from filled orbitals on one site to its neighbor and (*b*) the reciprocal process (**Figure 2*a***). Of course, the *d*-*d* charge transfer involves a sequence of *p*-*d* hops between the 2*p* ligand oxygen orbitals and the 3*d* transition metal orbitals (**Figure 2*b***). The σ overlap between the O-2*p* and e_g orbitals is stronger than the π overlap between O-2*p* and t_{2g} orbitals, and $t_{pd\pi} \sim (1/2)t_{pd\sigma}$. The exchange energy *J*, which varies as t_{pd}^4, is thus approximately 16 times larger for interactions involving e_g orbitals compared with t_{2g} orbitals between two neighboring *B*-site cations.

The *d*-*d* charge transfer is not necessarily the lowest-lying charge excitation. It competes with O-2*p*–*B*-3*d* charge transfer Δ, which is defined as

$$\Delta = E(d^{n+1}\underline{p}^5) - E(d^n\underline{p}^6). \quad 3.$$

The charge transfer gap can also localize electrons for $U > \Delta > t_{dd}$ and leads to a charge transfer insulator (14). The difference between the two types of insulators is essentially a matter of where the holes created by the excitations live: in a *d*-like orbital for a Mott-Hubbard insulator and in a 2*p*-like orbital for a charge transfer insulator. In perovskites with 3*d* transition metal cations, $U < \Delta$ for elements with lower atomic number (like Ti), whereas for higher oxidation states like Mn^{4+}

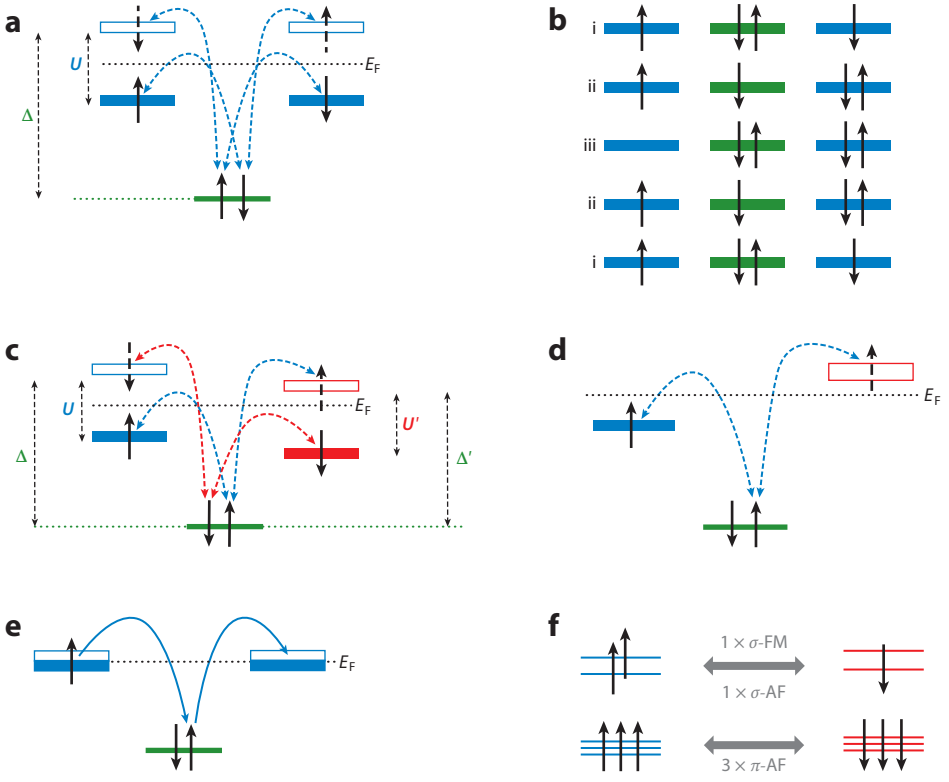

Figure 2

(*a*) Antiferromagnetic (AF) superexchange mediated through the ligand oxygen between two singly occupied orbitals through a 180° *B*-O-*B* bond. The dashed blue arrows indicate virtual hops back and forth from occupied to unoccupied states. Unoccupied states for a second electron on a given orbital are depicted as open boxes above the Fermi level (E_F) (*dotted black line*). The Pauli principle dictates that an electron virtually excited to this state have a spin opposite to that of the existing electron in the same orbital. (*b*) The sequence of configurations for one-half of the superexchange interaction in panel *a*, when a spin-up electron makes a virtual hop from the left *B*-site to an excited state on the right *B*-site and back. The equivalent reciprocal virtual hop from an occupied spin-down state on the right site to the left site is not shown. (*c*) AF superexchange at a *B*-O-*B′* bond, where we consider the energy level mismatch between *d* orbitals on *B* and *B′*. Here, a virtual hop from left to right (*dashed blue arrows*) is inequivalent to the reciprocal process from right to left (*dashed red arrows*). (*d*) Ferromagnetic (FM) superexchange at a *B*-O-*B′* interface, where *B* is occupied and *B′* is unoccupied in an insulating oxide. (*e*) Double exchange involves hopping between sites with a noninteger average occupancy per orbital, typically in a mixed-valence compound. The hopping leads to delocalized electrons and aligns the localized core spins on neighboring sites (not shown) via Hund's coupling to the itinerant electron spins. (*f*) Superexchange between a $3d^5$ site and a $3d^4$ site. The interactions between the three filled t_{2g} orbitals are π-AF. The interaction between the filled e_g orbital and the empty e_g orbital is σ-F. The interaction between the two filled e_g orbitals is σ-AF. The sum over all interactions is shown as AF.

and for elements further to the right in the periodic table like Ni and Cu, $U < \Delta$, yielding charge transfer insulators. The literature provides values for U and Δ for 3*d* transition metals (15). For exchange interactions, the charge transfer process involves virtual excitations of electrons from the O-2*p* orbital to the singly occupied *d* orbitals. In this case, $1/U$ in Equation 2 can be substituted by $1/\Delta$ in the simplest picture. Mott-Hubbard and charge transfer processes must

always be considered in parallel, with one dominating the other in limiting cases: Mott-Hubbard for $\Delta \gg U$ and charge transfer for $U \gg \Delta$.

These concepts can be extended to B-O-B' interactions at interfaces where the two transition metals are not the same and where the d orbitals on both cations are singly occupied (12). We consider only the Mott-insulating limit for brevity, for which $\Delta \gg U$. **Figure 2*c*** shows the case for singly occupied cations. Starting with Equation 2, we consider the two reciprocal processes that are now inequivalent due to the offset in levels between the B and B' cations. These processes lead to two terms:

$$J = \frac{-t_{dd'}^2}{U'} + \frac{-t_{d'd}^2}{U}, \qquad 4.$$

where $t_{dd'} = (t_{pd}t_{pd'})/\Delta'^2$ and for the reciprocal hop $t_{d'd} = (t_{pd'}t_{pd})/\Delta^2$ (**Figure 2*c***).

Ferromagnetic Superexchange

The most common way in which ferromagnetic (FM) superexchange occurs is when the interaction involves an occupied orbital and an empty orbital in an insulator, for instance, in the double perovskite La_2MnNiO_6. **Figure 2*d*** shows the process for a virtual hop between a singly occupied orbital on B and an unoccupied orbital on B'. The cost of adding an electron to the empty orbital on B' is U'. The energetic advantage of a FM alignment over an AF one is due to the Hund's energy J'_{H} on B' and is given by

$$J = t_{dd'}^2 \left[\frac{1}{(U' - J'_{\mathrm{H}})} - \frac{1}{(U')} \right] = t_{dd'}^2 \left[\left(\frac{1}{U'} \right) \frac{J'_{\mathrm{H}}}{(U' - J'_{\mathrm{H}})} \right]. \qquad 5.$$

Here, there is only one channel per orbital for interaction compared with two per orbital in Equation 4. Because $J_{\mathrm{H}} \sim 0.8$ eV, these interactions are weaker than the AF superexchange in Equation 4 by a factor of ~5.

Another form of FM superexchange can happen for a 90° B-O-B bond (e.g., in $LiNiO_2$ or CuO_2 chains) when the d orbitals on both cations are singly occupied. Any deviation from an 180° angle in an AF B-O-B' bond will mix in the 90° FM interaction, although in pseudocubic structures this effect is very weak and can be ignored to a first approximation.

Double Exchange

A second type of exchange, known as double exchange (**Figure 2*e***), involves a real hop of an electron between orbitals in neighboring transition metal cations (16). As in superexchange, the transfer involves a sequential hop of an electron from the oxygen to a transition metal and from a neighboring transition metal orbital to the oxygen. However, unlike superexchange, in which the electrons are localized, double exchange favors delocalization of carriers, long-range FM order, and metallicity. If the core spins on the B-cations are sufficiently large and $J_{\mathrm{H}} \gg t_{dd}$, the itinerant electron's spin is aligned parallel to the core spins on the transition metal sites, giving rise to a strong FM interaction (17). Double exchange has an angular dependence that varies as $\cos(\theta/2)$, where θ is the angle between the core spins (here we consider only $0° < \theta < 180°$). This angular dependence is like that in a spin valve in which parallel alignment between neighboring spins favors itinerancy, whereas the opposite is true for antiparallel spins. The strength of double-exchange interaction is nominally proportional to the number of itinerant carriers, which varies with doping, and to the bandwidth for charge transport, which is proportional to t_{dd}. The inclusion of both superexchange [which varies as $\cos(\theta)$] and double exchange in the simplest models for a cubic lattice results in a rich phase diagram including ferromagnetism, antiferromagnetism, and the famously elusive canted states (18). At an interface with competing magnetic interactions, the overall magnetic

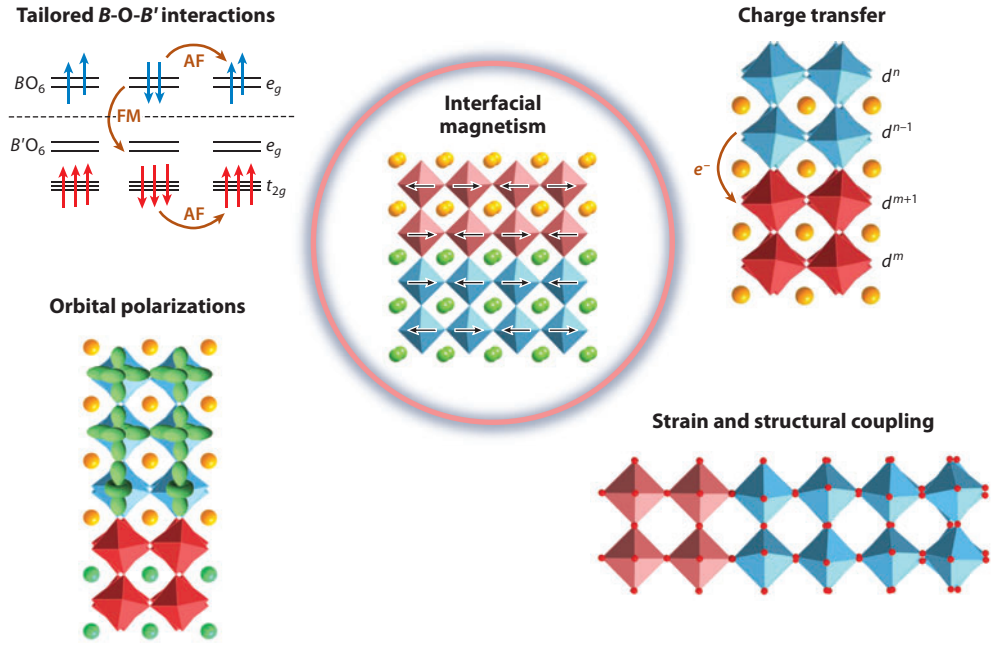

Figure 3

The ability to realize abrupt heterojunctions enables numerous mechanisms by which magnetism at interfaces can be modified. Four intrinsic mechanisms are illustrated: tailoring of *B*-O-*B′* bonding configurations across an interface to control local exchange interactions, interfacial charge transfer to alter electronic occupancy at interfaces, orbital polarizations and reconstructions, and strain and structural coupling to modify distortions and rotations of the BO_6 octahedra. Abbreviations: AF, antiferromagnetic; FM, ferromagnetic.

structure is that which minimizes the total exchange energy when summed over all neighboring cations, where each nearest-neighbor interaction is the sum over all exchange pathways (**Figure 2*f***).

3. INTERFACIAL MAGNETISM IN OXIDE HETEROSTRUCTURES

The ability to form heterojunctions between oxides with dissimilar magnetic, electronic, orbital, and structural properties can give rise to modified or novel magnetic behavior. The changes in magnetism due to the formation of a heterostructure can be either spatially confined to an interface, for instance, due to interfacial charge transfer, or present throughout an entire film, as typically occurs in the case of strain-driven phenomena or in short-period superlattices in which the entire crystal effectively consists of interfaces. This section reviews the most common mechanisms (**Figure 3**) by which exchange interactions can be engineered or altered due to the formation of a heterointerface, including interfacial charge transfer (Section 3.1), structural modifications and orbital polarizations (Section 3.2), tailored *B*-O-*B′* interactions obtained by cation ordering (Section 3.3), and reduced dimensionality (Section 3.4). Additionally, we describe how extrinsic effects such as point defects and intermixing can alter interfacial magnetism (Section 3.5).

3.1. Charge-Based Control of Interfacial Magnetism

As exchange interactions are sensitively dependent on orbital filling, modifications to the local electron count on the *B*-site cation can have significant consequences for magnetic ordering.

Here, we describe how interfacial charge transfer and field-effect-induced charge accumulation can alter magnetism at interfaces.

3.1.1. Interfacial charge transfer. Charge transfer at oxide interfaces has been one of the most popular pathways toward realizing new electronic and magnetic states in oxide heterostructures (19). In this approach, charge transfer occurs at an interface to equilibrate the difference in chemical potentials between carriers in the two materials, in analogy with interfaces in conventional semiconductors and metals. This has been proposed as a general method for interfacial doping at epitaxial interfaces between oxides (20) and is the focus of this section. One way in which interfacial charge transfer has been realized is modulation doping, in which the *A*-site composition is varied between different layers, whereas the *B*-site transition metal is kept the same (e.g., $La^{3+}Ti^{3+}O_3/Sr^{2+}Ti^{4+}O_3$ or $La^{3+}Mn^{3+}O_3/Sr^{2+}Mn^{4+}O_3$) (21–23). This process causes the nominal electron count on the transition metal to vary across an interface. If the *B*-site energy levels are appropriately aligned, the amplitude for hopping between them may be substantial and can cause charge to quantum mechanically leak across the interface. However, this comes at the cost of a Coulomb binding energy of $\sim e^2/(\varepsilon a)$ for leaving behind a hole, where ε is the dielectric function and a is the lattice spacing (24). This gives rise to a natural length scale for charge spreading across an interface, analogous to a Thomas-Fermi length in conventional metals, $L_{TF} \sim t(\varepsilon a^2/e^2)$, where t is the hopping amplitude. For typical material parameters in oxides ($\varepsilon \sim 15$, $t \sim 0.2$ eV), this length scale has been calculated to be ~1–3 unit cells (25). The amount of charge that leaks across an interface is such that the resulting electric field integrated over approximately L_{TF} yields the difference in chemical potentials between the two materials. This charge transfer causes the interfacial region, extending over a few unit cells, to have an electron count different from the bulk values of the two materials. Although the lineup between levels for $ABO_3/A'BO_3$ interfaces seems intuitively obvious, as it involves charge leakage between *B*-cations with different valences (eg. B^{3+}-O-B^{4+}), for $AB'O_3/ABO_3$ interfaces (e.g., $LaNiO_3/LaMnO_3$ or $LaTiO_3/LaMnO_3$) and $A'B'O_3/ABO_3$ interfaces (e.g., $SrTiO_3/LaMnO_3$), it is not so clear and must be inferred from experiment. For example, measurements of the Schottky barrier formed by various ABO_3 perovskites with degenerately doped *n*-$SrTiO_3$ have revealed trends in the variation of chemical potential with doping, as well as across different 3*d* transition metals on the *B*-site (26, 27). These experiments indicate that, as the *B*-site is occupied by transition metals with increasing atomic numbers, the chemical potential decreases for a given 3*d* occupation. These trends may be used as a guide to design charge transfer across interfaces. The literature on redox couples, in which one pair of oxidation states is preferred over the other, can also provide a useful guide. For example, the right-hand side of the reaction $Ni^{3+} + Mn^{3+} \rightarrow Ni^{2+} + Mn^{4+}$ is believed to be energetically favored (28).

Experimentally, when charge transfer occurs, it can change the nature of magnetic interactions and transport properties of the interfacial region. For example, near the interface between the AF insulators $LaMnO_3$ and $SrMnO_3$, the electron count is intermediate between $3d^4$ and $3d^3$ over a region of several unit cells, which can favor double-exchange ferromagnetism. Thus, one can obtain quasi-two-dimensional ferromagnetism at the interface between two AF insulators. Although ferromagnetism is sensitive to structural issues such as interfacial roughness, this concept has been realized (**Figure 4**) and verified with photoemission (30), transport (31, 32), and optical conductivity (33) measurements. Because the GKA rules depend on the number of electrons in orbitals participating in exchange interactions, changes in orbital occupancy with interfacial charge transfer can also give rise to new types of magnetic interactions. Polarized X-ray scattering results showed that, in large-period $(LaMnO_3)_{2n}/(SrMnO_3)_n$ superlattices ($n > 5$), the

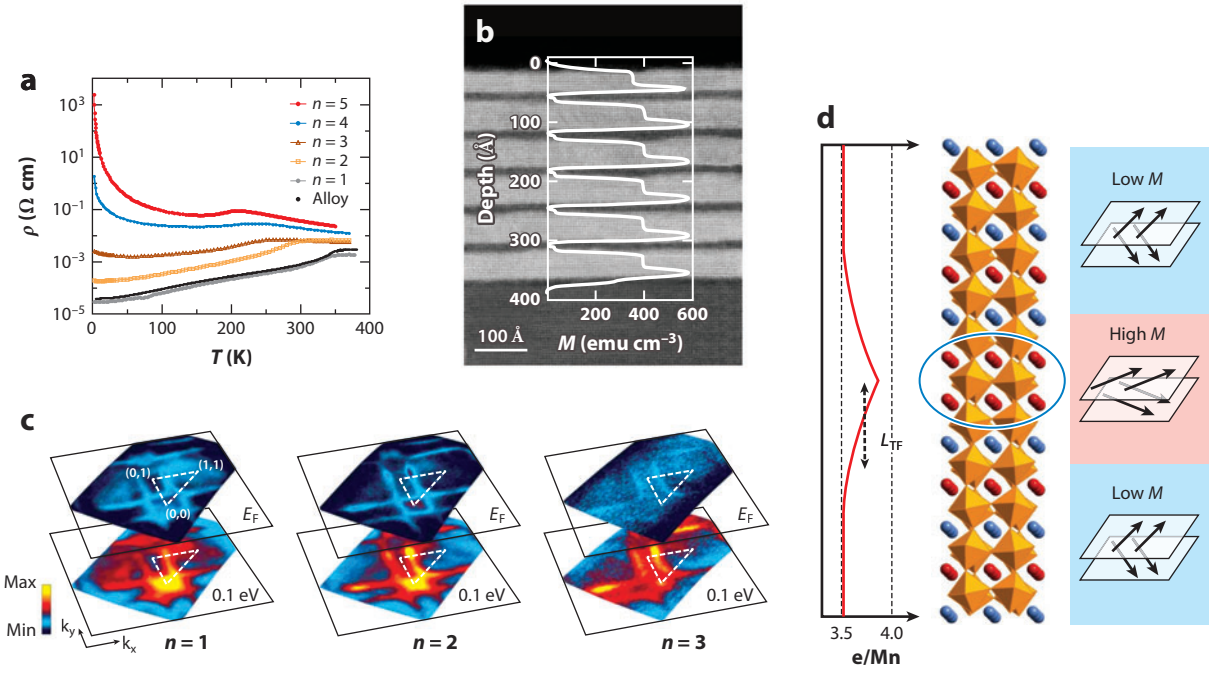

Figure 4

(*a*) Metal-insulator transition in $(LaMnO_3)_{2n}/(SrMnO_3)_n$ superlattices with increasing n, where the superlattices are insulating for $n > 3$ and metallic for $n < 3$. Reproduced from Reference 31. Copyright 2008, American Physical Society. (*b*) Modulated magnetization as measured with polarized neutron reflectometry in a large-period $(LaMnO_3)/(SrMnO_3)$ insulating superlattice. The *Z*-contrast scanning transmission electron microscope image of the superlattice shows that the bright regions correspond to $LaMnO_3$ and that the dark regions correspond to $SrMnO_3$, due to the higher atomic number (*Z*) of the La atom columns. The magnetization is strongly suppressed in $SrMnO_3$. In this particular sample, interfaces alternate, on average, between smooth and rough. Rough interfaces have lower magnetization than do smooth interfaces. Adapted with permission from Reference 29. Copyright 2008, American Physical Society. (*c*) Photoemission experiments from a series of $(LaMnO_3)_{2n}/(SrMnO_3)_n$ superlattices. The spectral weight at the Fermi surface is strongly reduced going from the metallic $n = 1$ superlattice to the insulating $n = 3$ superlattice. The two maps for each superlattice are at the Fermi level (E_F) and at a binding energy of 0.1 eV below E_F. Reproduced with permission from Reference 30. Copyright 2012, Nature Publishing Group. (*d*) Delta doping of ferromagnetism within an antiferromagnetic manganite. The left panel shows a schematic of the charge distribution in the delta-doped $LaMnO_3/SrMnO_3$ superlattice that is shown in the middle panel. The spins are canted, with the angle between spins at 157° in the low-moment regions and at 103° in the high-moment regions (*right panel*). Adapted with permission from Reference 40. Copyright 2011, American Physical Society.

orbital occupancy was distinct in the bulk of $LaMnO_3$ compared with that at the interface (34). This difference in orbital polarization was accompanied by a change in the anisotropy of spins in the vicinity of the interfaces compared with the bulk of $LaMnO_3$.

In short-period $ABO_3/A'BO_3$ superlattices, in which the period is smaller than or comparable to L_{TF}, the charge spreads out between the layers, and all *B*-site cations have a nominal valence set by the composition of the superlattice, e.g., $Mn^{3.67+}$ for $(LaMnO_3)_2/(SrMnO_3)_1$ superlattices, which yields a FM metallic phase. This phase is realized without the *A*-site cation disorder that accompanies the usual doping strategies in bulk single crystals. The absence of cation disorder can have important consequences for phases that are sensitive to this kind of disorder. For example, in $(LaMnO_3)_n/(SrMnO_3)_{2n}$ superlattices, the AF Néel temperature (T_N) was enhanced compared with that of a random alloy of $La_{0.33}Sr_{0.67}MnO_3$ by approximately 70 K from ~250 K to 320 K (35). This enhancement was presumably due to the fact that at this composition, the bulk material has

two competing AF states: an A-type (layered) AF state and a C-type (chain-type) AF state (36). At first-order phase boundaries between such phases, there are theoretical predictions of enhanced sensitivity of the ordering temperature to disorder (37). Such competing electronic/magnetic phases are found in many transition metal oxides. Mitigating the effects of disorder by cation ordering may thus be a general strategy by which to obtain enhanced transition temperatures or other new properties in magnetic oxides.

The precise placement of dopants in a lattice may enable other effects that are not observable in bulk samples. As an example, theoretical calculations show that the homogeneously canted AF phase that arises as a result of the competition between double exchange and superexchange in manganites is fundamentally unstable to phase separation between FM and AF regions (38). However, by using a delta-doping approach (**Figure 4*d***) (39), a canted AF state could be realized within an A-type AF host (40). In these superlattices, epitaxial constraints may be responsible for stabilizing the canted AF state. In principle, this quasi-two-dimensional FM metal may be tuned with a gate electric field.

3.1.2. Electrostatic charge accumulation/depletion. The interfacial electronic configuration can also be modified by using electrostatic field-effect gating (41), providing a route for controlling interfacial magnetism with electric fields. The use of ferroelectrics such as $Pb(Zr_{0.2}Ti_{0.8})O_3$ (PZT) or electrolytic polymers and liquids as alternative gate dielectrics enables the accumulation of carrier concentrations on the order of 10^{14} cm^{-2} (42, 43), significantly higher than those that can be achieved by using conventional dielectric oxides. These levels of induced charge can alter the nominal valence of the *B*-site cation in the few unit cells nearest the interface, producing changes in the saturation magnetization and in the stability of FM-versus-AF exchange interactions. Recent work on PZT/$La_{0.8}Sr_{0.2}MnO_3$ field-effect structures provided an example of this approach. By switching the polarization of the PZT with the application of an electric field, an accumulation or depletion of carriers was achieved in the interfacial region of the manganite layer, leading to bias-dependent and reversible changes in the Curie temperature (T_C) and magnetization of $La_{0.8}Sr_{0.2}MnO_3$. X-ray absorption spectroscopy measured at the Mn $L_{2,3}$ edge during biasing revealed a shift of 0.3 eV between depletion and accumulation; this shift corresponded to approximately 0.1 electrons per Mn in the near-interfacial region (44). The measured change in magnetization between the two biasing conditions was ~0.76 μ_B per Mn, significantly larger than the value of 0.1 μ_B per Mn expected if the effect on magnetism was limited solely to a change in the number of unpaired *d* electrons. Instead, this discrepancy suggested that the relative magnitudes of the exchange interactions are altered via electrostatic doping, for instance, weakening the FM (AF) exchange while enhancing AF (FM) interactions, an effect also captured in density functional theory studies of manganite/ferroelectric interfaces (45).

3.2. Structure- and Orbital-Driven Control of Magnetism

The strong coupling between atomic structure and magnetic properties has been well established in bulk perovskites (46, 47), including clear demonstrations of how ordering temperatures and magnetic ground states are highly sensitive to *B*-O-*B* bonding environments because electronic bandwidth is dependent on metal-oxygen bond lengths and angles. Thin films provide the opportunity to realize nonbulklike crystal structures through epitaxial stabilization and to alter the metal-oxygen bond environments and *d* orbital polarizations via substrate-induced strain, which can result in films with magnetic properties quite different from those of their isocompositional bulk counterparts. Additionally, interfacial structural coupling and orbital reconstructions can induce novel magnetic behavior confined to length scales of a few unit cells at an interface.

3.2.1. Epitaxial stabilization. In epitaxial stabilization, a metastable phase becomes preferable to the equilibrium phase due to an energy reduction at the film/substrate interface (48). The growth of hexagonal manganite films offers a good example of epitaxial stabilization as applied to complex oxides. In bulk, rare earth manganites with relatively large *A*-site cations, such as $LaMnO_3$, exhibit an orthorhombic perovskite structure with corner-connected MnO_6 octahedra. However, the substitution of smaller *A*-site cations, such as in $LuMnO_3$, leads to a hexagonal structure with MnO_5 trigonal bipyramids (49). In rare earth manganites in which the *A*-site ionic radii are between La and Lu, for instance, $HoMnO_3$ or $DyMnO_3$, the energetic difference between the two different crystal structures becomes small. For such compounds, the hexagonal or orthorhombic structures can be manifested through the choice of substrate. For example, whereas $GdMnO_3$ is orthorhombic in bulk, films grown on (111)-oriented $(ZrO_2)_{0.85}(Y_2O_3)_{0.15}$ or hexagonal $YMnO_3$ substrates can be stabilized in the hexagonal structure (50, 51). Above a critical thickness, the interfacial energy reduction is offset by the larger enthalpy of the hexagonal phase compared with that of the orthorhombic phase, causing the film structure to revert back to orthorhombic (50). Similarly, hexagonal manganites can be stabilized in pseudocubic perovskite structures; an example is $YMnO_3$. Orthorhombic $YMnO_3$ films have attracted considerable interest due to their multiferroic behavior, including the presence of AF and cycloidal magnetic order (52–54).

Epitaxy can also be used to stabilize the perovskite structure in films in which the cations are forced into unfavorable valence states, as in the case of $EuMoO_3$. Bulk high-pressure synthesis resulted in the pyrochlore $Eu_2Mo_2O_7$, which displays the preferred valence states of the cations Eu^{3+} and Mo^{4+}. By using pulsed laser deposition, epitaxial $EuMoO_3$ films were stabilized on $GdScO_3$ substrates with a $SrTiO_3$ buffer layer (55). $EuMoO_3$ films, in which Eu takes on a 2+ valence, are metallic ferromagnets.

3.2.2. Epitaxial strain. When pseudocubic perovskite films are grown on pseudocubic perovskite substrates, epitaxial strain can have a profound effect on the BO_6 bonding environment, as the substrate in-plane lattice parameters are imposed on the film, resulting in BO_6 distortion and/or rotations that are quite different from those found in compositionally equivalent bulk compounds (56). Given that magnetic ordering and transition temperatures in perovskites depend sensitively on the *B*-O lengths and on the *B*-O-*B* angles (46, 47, 57), modifying octahedral distortions and rotations in films provides a means by which to engineer magnetism in oxide heterostructures. Indeed, multiple studies have shown that epitaxial strain can dramatically alter magnetic properties by suppressing ferromagnetism, inducing FM states in otherwise paramagnetic materials, and altering the stability of magnetic ground states. In this way, epitaxial strain enables isocompositional films to be realized with either FM or AF structures.

The mixed-valence manganites have been a model system for investigations of how epitaxial strain can alter magnetism. The magnetic properties of bulk manganites, such as $La_{1-x}Sr_xMnO_3$ and $La_{1-x}Ca_xMnO_3$, have received considerable attention due to their rich phase diagrams in which multiple magnetic ground states are present and competition between neighboring phases can give rise to colossal responses (36). **Figure 5** illustrates three AF orderings—A type, C type, and G type—found in manganites and other magnetic perovskites.

Strain-induced changes in the magnetic properties of manganites are driven largely by two coupled effects: (*a*) the modification of *B*-O bond lengths and *B*-O-*B* bond angles and (*b*) the creation of an orbital polarization favoring occupancy of either the $d_{x^2-y^2}$ or $d_{3z^2-r^2}$ orbitals (**Figure 6*a***) (58–62). The former effect produces changes in the hopping probability between adjacent heterovalent *B*-site cations, altering the strength of FM exchange interactions. Similarly, AF superexchange interactions are also sensitive to bond lengths and angles (both depend on t_{dd}). Strain-induced orbital polarizations also result from alterations to the local bonding environment.

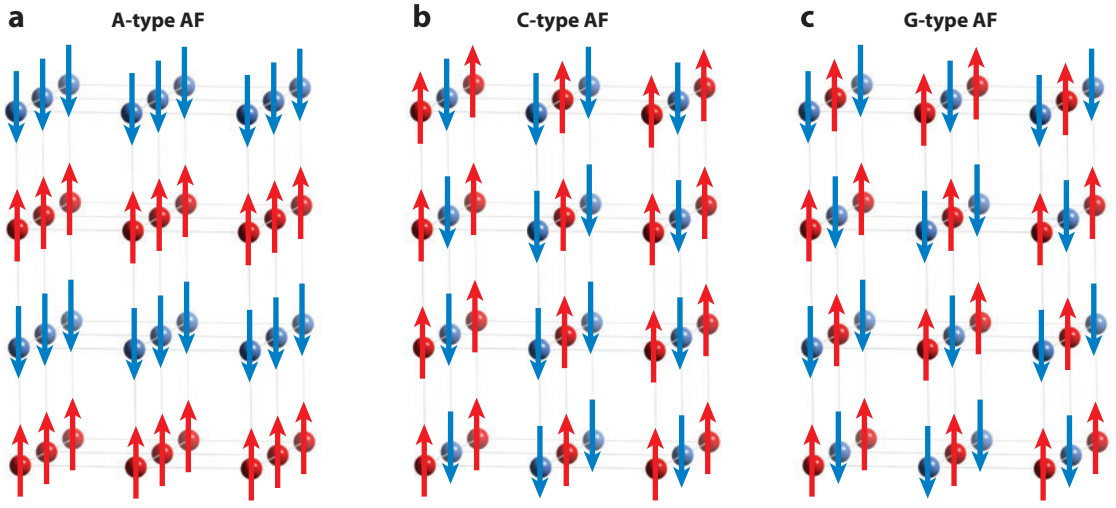

Figure 5

Schematics showing the arrangement of spins in (*a*) A-type, (*b*) C-type, and (*c*) G-type antiferromagnets (AF). For clarity, only the *B*-site sublattice of the perovskite structure is shown. The red and blue colors denote spin up and spin down, respectively.

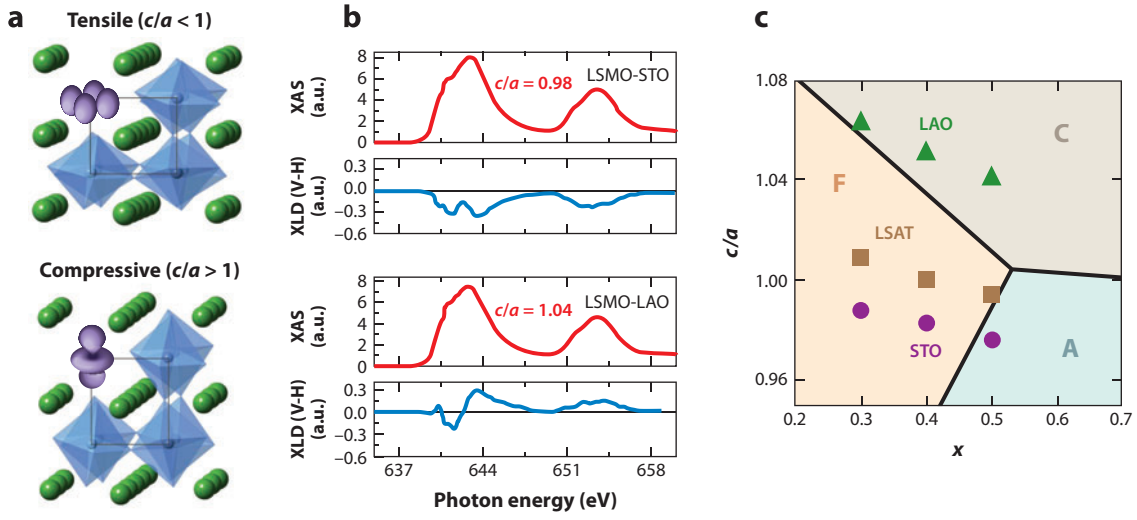

Figure 6

(*a*) The preferred orbital occupations arising from a difference in the *B*-O bond lengths along the in- and out-of-plane directions are shown schematically. Tensile strain ($c/a < 1$; *top*) favors a $d_{x^2-y^2}$ orbital polarization, whereas compressive strain ($c/a > 1$; *bottom*) favors a $d_{3z^2-r^2}$ orbital polarization. (*b*) These orbital polarizations can be measured by using X-ray linear dichroism (XLD), in which the differential absorption of vertically and horizontally (V-H) polarized X-rays is measured as the photon energy is scanned through a *B*-site or oxygen absorption edge. For example, XLD has been used to measure these orbital polarizations in $La_{0.7}Sr_{0.3}MnO_3$ (LSMO) films on $SrTiO_3$ (STO) (tensile strain) and on $LaAlO_3$ (LAO) (compressive strain). XAS denotes X-ray absorption spectroscopy. Panel *b* is adapted with permission from Reference 63. Copyright 2006, American Physical Society. (*c*) The phase diagram of strained $La_{1-x}Sr_xMnO_3$ films reveals how strain-induced orbital polarizations can be used to tune the spin structure between ferromagnetic (F) and A- and C-type antiferromagnetic orderings. The symbols correspond to films grown on LAO, (La,Sr)(Ta,Al)O_3 (LSAT), and STO substrates. Panel *c* adapted with permission from Reference 59. Copyright 1999, Physical Society of Japan.

In perovskites, the e_g orbitals are elongated toward the O-2*p* orbitals, increasing the energy of the e_g states relative to t_{2g} orbitals, which do not point directly at the O-$2p_\pi$ orbitals. The Coulomb interaction of the e_g orbitals can be further modified through changes to the *B*-O bond lengths. Tensile strain, which extends the in-plane *B*-O bond and contracts the out-of-plane *B*-O bond, reduces the energy of the $d_{x^2-y^2}$ orbital relative to the $d_{3z^2-r^2}$ orbital, leading to an enhanced occupation (often referred to as an orbital polarization) of the $d_{x^2-y^2}$ states. Similarly, compressive strain produces a $d_{3z^2-r^2}$ orbital polarization. Experimentally, these orbital polarizations can be probed by using soft-X-ray linear dichroism, an example of which is shown in **Figure 6*b*** (63).

$La_{0.7}Sr_{0.3}MnO_3$ (LSMO) is a canonical double-exchange ferromagnet, and numerous studies have investigated the effect of strain on its magnetic properties. Adamo and coauthors (64) grew LSMO films on nine different substrates, spanning strains from −2.3% compressive to 3.2% tensile. Both compressive and tensile strain states suppressed T_C in a manner consistent with previous theoretical work of Millis et al. (58), in which the strain dependence of T_C was modeled by considering the effects of lattice distortions on the Jahn-Teller splitting and on the electron hopping amplitude. The use of piezoelectric substrates, with which the strain can be controlled by an external bias, has enabled studies of how strain alters magnetic behavior in a single LSMO film. Changes to the strain state of only 0.1% shifted T_C by 19 K, illustrating the sensitivity of magnetism to subtle structural modifications (65). In FM manganites, strain and the symmetry of the substrate also play a critical role in a film's magnetic anisotropy (66, 67).

With increased Sr (or Ca) composition, the orbital polarization induced by strain begins to play a critical role in the magnetic ground state of manganite films. In bulk manganites, a crossover from FM order to AF order typically occurs near half-doping of trivalent and divalent *A*-site cations, making this region of the phase diagram susceptible to phase competition between FM and AF behavior. For thin films, the close proximity of these phases provides an intriguing region of the phase diagram in which to explore how orbital polarization can be used to control magnetism. The preferential occupation of the $d_{x^2-y^2}$ orbitals induced by tensile strain allows for FM in-plane interactions between full and empty $d_{x^2-y^2}$ states and AF out-of-plane interactions between full t_{2g} states. This combination of exchange interactions results in A-type antiferromagnetism. In contrast, a $d_{3z^2-r^2}$ orbital polarization induced by compressive strain promotes out-of-plane FM interactions and in-plane AF interactions, leading to C-type antiferromagnetism. Konishi and coauthors (59) demonstrated this strategy of using orbital occupancy to tailor the spin structure. These authors produced a phase diagram of the magnetic ordering as a function of strain and composition (**Figure 6*c***) on the basis of experimental measurements of strained $La_{1-x}Sr_xMnO_3$ films. Subsequent density functional theory calculations reproduced the essential features of the phase diagram while also expanding the range of compositions and strain states (60). More recent neutron diffraction measurements confirmed the presence of the A-type AF ordering type in tensile-strained $La_{0.5}Sr_{0.5}MnO_3$ on $SrTiO_3$ (39).

Strain-induced transitions between ordered spin structures are not limited to manganite films. $EuTiO_3$, when grown on different substrates, exhibits a transition between FM and AF orderings (68), although the origin of this behavior lies in biquadratic spin-lattice coupling (69) as opposed to e_g orbital polarization effects.

In some cases, epitaxial strain has been used to coax magnetic ordering out of materials that otherwise exhibit paramagnetic behavior in their equilibrium structures. An example material exhibiting a strain-induced paramagnetic-to-FM transition is $LaCoO_3$, which lacks an ordered magnetic ground state in bulk form. Numerous groups have reported ferromagnetism in insulating $LaCoO_3$ films under tensile strain, with a consistent T_C of ∼85 K (70–72). The application of epitaxial strain also promotes the high and/or intermediate spin state and suppresses the spin state transition observed in bulk $LaCoO_3$ (73, 74). The origin of ferromagnetism in strained $LaCoO_3$

remains the subject of intense ongoing investigations. Proposed mechanisms include the ordering of high- and low-spin Co^{3+} that leads to FM superexchange (75), a canted spin structure due to competing exchange interactions in an ordered high- and low-spin state (76), and the presence of an orbitally ordered intermediate- and high-spin superstructure (77).

3.2.3. Interfacial structural coupling and orbital reconstructions. Depending on the magnitude of lattice mismatch, perovskite films can remain coherently strained for up to tens of unit cells. In addition to strain, a symmetry mismatch or a difference in the magnitude of octahedral rotations at a coherent heterointerface provides a second means by which to alter local atomic structure. To maintain the corner connectivity of the BO_6 octahedra across an interface, the octahedral rotations near a perovskite heterointerface are modified. For instance, rotations are suppressed in the near-interfacial region of orthorhombic or rhombohedral perovskites epitaxially constrained to cubic perovskites (78–81). In contrast to the length scales associated with strain, the length scales associated with coupling of octahedral rotations and distortions across heterointerfaces are much shorter: on the order of one to ten unit cells (78, 79, 82–85).

Recent studies of $(GdTiO_3)_n/(SrTiO_3)_{13}$ superlattices (86), enabled by the application of the position-averaged convergent beam electron diffraction (PACBED) technique to oxide heterostructures (87), illustrate how changes to interfacial atomic structure can lead to magnetic behavior that would be otherwise unexpected on the basis of bulk phase diagrams. Rare earth titanates exhibit a transition from AF to FM behavior, with increasing *A*-site displacements and octahedral rotations induced by decreasing *A*-site cation size (88). Whereas bulk $GdTiO_3$ exhibits Gd displacements and octahedral rotations large enough to render it FM, the formation of a heterointerface with cubic $SrTiO_3$ suppresses these lattice distortions. By increasing n from 6 to 10, the distortions in $GdTiO_3$ are increasingly able to relax back to their bulk magnitudes (**Figure 7*a*,*b***). Via magnetometry and PACBED measurements performed on the same superlattices, the relationship between the magnetic properties and atomic structure in $GdTiO_3$ was determined, and these magnetic properties and atomic structures were compared with those of bulk titanates (**Figure 7*c–e***). Surprisingly, ferromagnetism is present in $GdTiO_3$ layers even where the distortions are quenched to magnitudes comparable to those of bulk AF $LaTiO_3$, suggesting that the orbital order believed to play a critical role in the FM behavior can be sustained in confined layers despite significant reductions to the lattice distortions (86).

Similar to the case of how interfacial structural coupling can alter octahedral behavior over a length scale much shorter than that of epitaxial strain, the orbital behavior at an oxide interface or surface can be modified in a manner distinct from that of strain-induced orbital polarization. This phenomenon, in which the surface or interfacial orbital occupancy differs from that of the noninterfacial region of a material, is referred to as an orbital reconstruction (89). Orbital reconstructions can give rise to novel magnetic states and to coupling between dissimilar perovskites, as demonstrated in heterojunctions of AF $BiFeO_3$ (BFO) and FM LSMO (90). X-ray magnetic circular dichroism (XMCD) measurements revealed the presence of a FM moment on interfacial Fe cations at temperatures less than ~100 K, coupled antiferromagnetically to the magnetization direction of LSMO. Concurrent with the onset of this interfacial magnetization, the energy of the Fe $d_{3z^2-r^2}$ orbital decreased with decreasing temperature, in contrast to the slight increase in energies of the Fe $d_{x^2-y^2}$ and Mn e_g orbitals. This experimental observation was attributed to the hybridization of the Fe and Mn $d_{3z^2-r^2}$ states, leading to the formation of a bonding Fe $d_{3z^2-r^2}$ orbital and of an antibonding Mn $d_{3z^2-r^2}$ orbital at the interface. The increased energy of the Mn $d_{3z^2-r^2}$ orbital produces a $d_{x^2-y^2}$ orbital polarization on the interfacial Mn cations. The authors (90) hypothesized that this orbital reconstruction leads to AF coupling between the interfacial LSMO and the noninterfacial LSMO, which can be thought of as two layers of A-type, antiferromagnetically

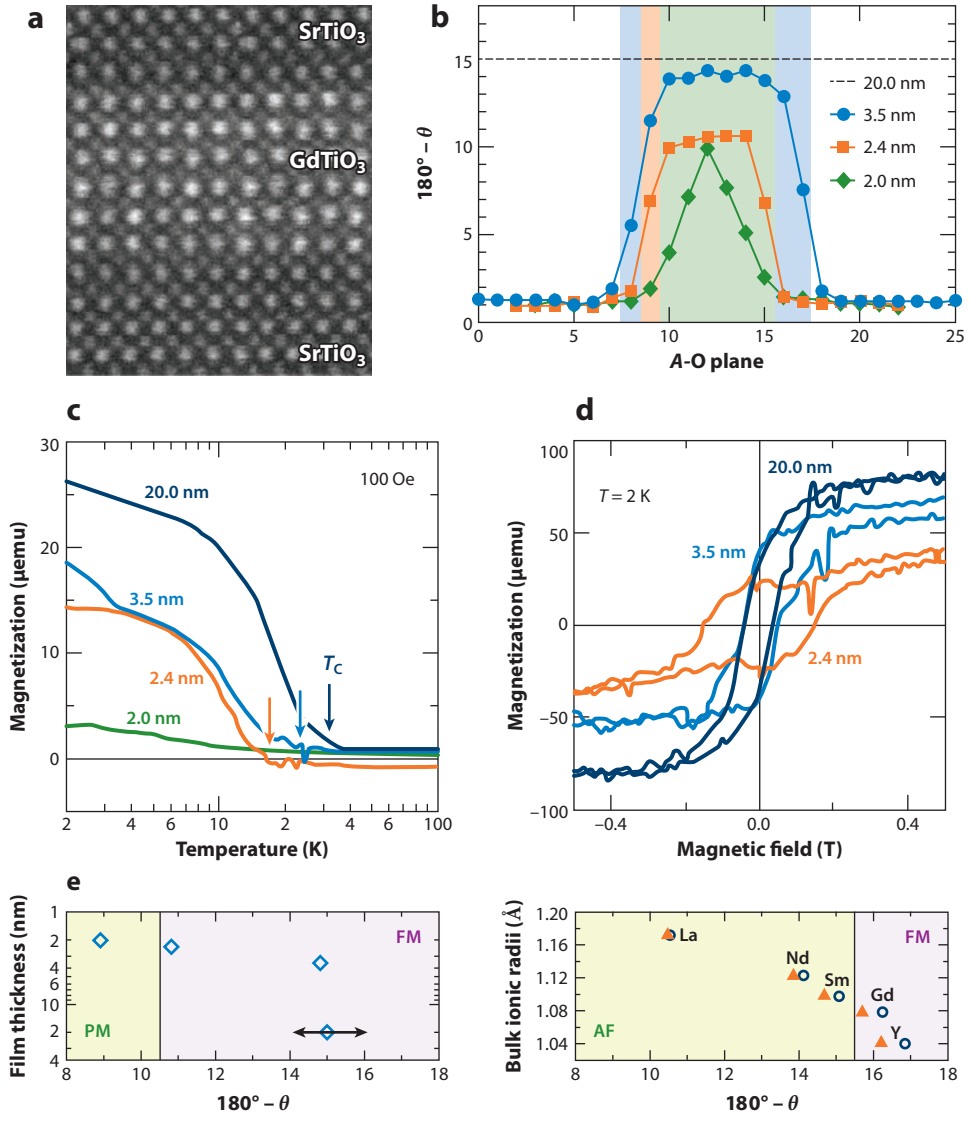

Figure 7

The case of $GdTiO_3$ confined between $SrTiO_3$ provides an example of how understanding interfacial atomic structure can yield new insights into magnetic behavior. (*a*) A scanning transmission electron microscopy image of a sample with a 2-nm $GdTiO_3$ layer is shown. (*b*) The angles between three successive Gd/Sr cations, which act as a measure of the *A*-site displacement and relative magnitude of octahedral tilts, are shown as a function of distance through $GdTiO_3$ for different layer thicknesses. The structural distortion is suppressed as $GdTiO_3$ thickness is reduced. (*c–e*) Combining the measured magnetic properties (*c*,*d*) with the structural information enables comparison of confined $GdTiO_3$ and bulk $GdTiO_3$ (*e*). Abbreviations: AF, antiferromagnetic; FM, ferromagnetic; PM, paramagnetic. Reproduced with permission from Reference 86; copyright 2013 by American Physical Society.

ordered LSMO. The interactions between the occupied interfacial Fe $d_{3z^2-r^2}$ orbital and the empty interfacial Mn $d_{3z^2-r^2}$ orbital produce a FM exchange between the interfacial BFO and LSMO. In this scenario, the FM exchange between the Fe and Mn is accommodated by a canting of the spins in BFO near the interfaces, leading to the net FM moment observed in XMCD. Calderón and coauthors (91) reproduced the Mn $d_{x^2-y^2}$ orbital polarization at the interface by using a model Hamiltonian. The calculations also reproduced the net magnetization in the top BFO layer, coupled antiferromagnetically to the LSMO, which did not deviate from FM behavior, even at the interface. A second example of orbital reconstructions playing a key role in interfacial magnetism is the $La_{0.7}Ca_{0.3}MnO_3/YBa_2Cu_3O_7$ system, in which a net magnetic moment oriented antiparallel to the Mn moment is observed on the Cu atoms (92). An orbital reconstruction—in which the holes in the interfacial cuprate layer partially occupy the $d_{3z^2-r^2}$ orbital, in contrast to their bulk behavior—is believed to play a critical role in stabilizing the interfacial magnetism (89).

3.3. Controlling Local *B*-O-*B′* Exchange Interactions at Interfaces

The ability to form abrupt $(ABO_3)/(AB'O_3)$ interfaces allows the local magnetic exchange interactions to be designed by controlling the number of *B*-O-*B*, *B*-O-*B′*, and *B′*-O-*B′* bonds. This approach is particularly powerful in the case of $(ABO_3)_1/(A'B'O_3)_1$ superlattices, offering a route to stabilize spin structures not observed in compositionally equivalent bulk compounds. To illustrate the general approach, consider the case in which both ABO_3 and $AB'O_3$ are G-type antiferromagnets, all *B*-O-*B* and *B′*-O-*B′* bonds produce AF interactions, and the *B*-O-*B′* coupling is FM. Taking advantage of these three bonds—AF *B*-O-*B*, AF *B′*-O-*B′*, and FM *B*-O-*B′*—the spin structure in $(ABO_3)_1/(AB'O_3)_1$ superlattices can be tailored by growing along different crystallographic directions without changing the overall cation composition. Deposition on a (001) substrate leads to alternating $BO_2/B'O_2$ (001) planes, as shown in **Figure 8*a***. In this superlattice, every *B* cation has two FM *B*-O-*B′* interactions along the [001] direction and four AF *B*-O-*B* interactions within the (001) plane. This leads to the C-type AF structure shown in **Figure 8*b***. In a (110)-oriented superlattice (**Figure 8*c***), every *B* cation has four FM *B*-O-*B′* interactions and two AF *B*-O-*B* interactions, producing the A-type AF structure (**Figure 8*d***). Finally, when grown on a (111) substrate, every *B* cation has six FM *B*-O-*B′* interactions and no *B*-O-*B* bonds (**Figure 8*e***). This arrangement, equivalent to a perfectly ordered double perovskite, yields a FM spin structure (**Figure 8*f***).

Ueda et al. (93, 94) reported experimental attempts to stabilize these different spin structures in superlattices, synthesizing $(LaFeO_3)_1/(LaCrO_3)_1$ superlattices grown on (001)-, (110)-, and (111)-oriented $SrTiO_3$ substrates. Both bulk $LaFeO_3$ and $LaCrO_3$ are G-type antiferromagnets, which can be understood by using the GKA rules. $LaFeO_3$ has a high-spin d^5 configuration, resulting in full-full e_g interactions and therefore AF coupling across all Fe-O-Fe bonds. Similarly, $LaCrO_3$ has a d^3 configuration with full-full t_{2g} (empty-empty e_g) interactions, leading to AF exchange across all Cr-O-Cr bonds. When these two compounds are brought together at an interface, Fe-O-Cr bonds are formed, producing FM full-empty e_g and AF full-full t_{2g} interactions. The magnetic coupling associated with this configuration leads to either ferro- or ferrimagnetism, depending on the relative strengths of the e_g and t_{2g} exchange interactions and the correlation energy U (95, 96). FM-like behavior was reported in the (111)-oriented superlattice, with a T_C of 375 K and a saturation moment of 2.5 μ_B per *B*-site (94). In contrast, (110)- and (001)-oriented superlattices exhibited temperature-dependent magnetization behavior consistent with antiferromagnetism. A similar result was obtained for $(BiFeO_3)_1/(BiCrO_3)_1$ superlattices (97). More recent studies of La_2FeCrO_6 films in which detailed X-ray measurements were used to quantify the degree of *B*-site ordering found ferrimagnetic behavior in highly ordered films with a T_C of ~50 K (98). The

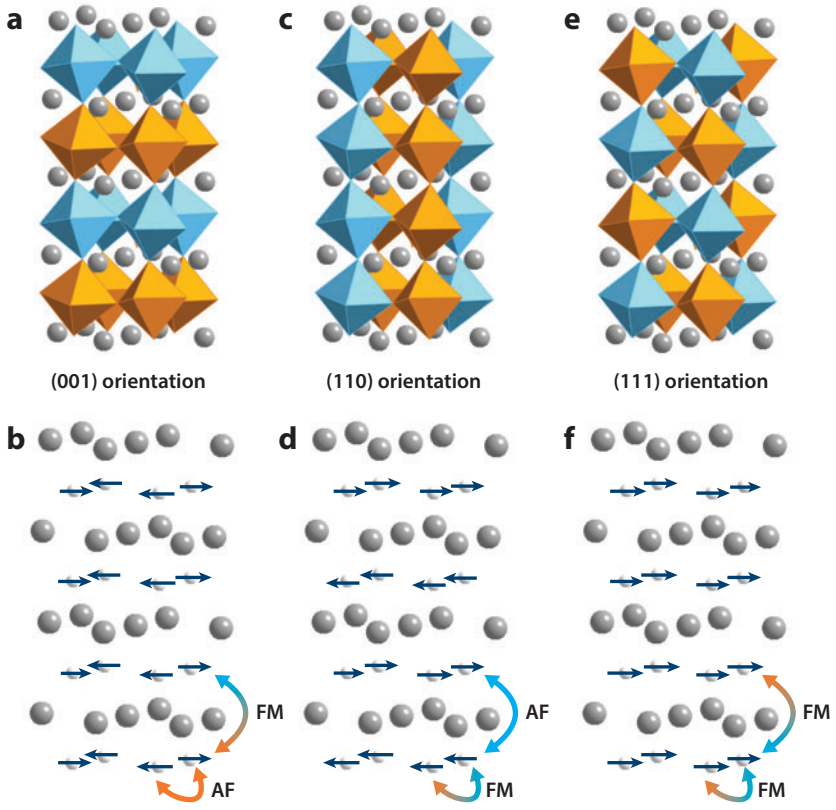

Figure 8

Schematic illustrating $(ABO_3)_1/(AB'O_3)_1$ superlattices grown along different orientations and the resultant spin structures, assuming antiferromagnetic (AF) *B*-O-*B*, AF *B′*-O-*B′*, and ferromagnetic (FM) *B*-O-*B′* interactions. Growth on (*a*) (001)-oriented, (*c*) (110)-oriented, and (*e*) (111)-oriented substrates produces (*b*) C-type AF, (*d*) A-type AF, and (*f*) FM spin structures, respectively. The *A*-site cations are represented by gray spheres. In panels *a*, *c*, and *e*, the BO_6 and $B'O_6$ octahedra are blue and orange, respectively.

saturation moment depended strongly on the degree of ordering, transitioning from $M_S = 1\ \mu_B$ per *B*-site in ordered films, as expected for a ferrimagnetic ground state, to the loss of a magnetic moment with increasing disorder.

Control of exchange interactions in *B*-site-ordered superlattices has been investigated in material systems beyond $(LaFeO_3)/(LaCrO_3)$. The magnetic properties of nickelate/manganite (99–102), ferrite/manganite (103–105), and chromate/manganite (99) superlattices in which the *A*-site valence is uniform have been analyzed in the context of local exchange couplings. However, in some of these cases, interfacial charge transfer plays a key role in the sign and magnitude of the exchange interactions, adding an additional layer of complexity to the magnetic behavior.

More intricate magnetic orders may be achieved by tuning the superlattice composition, *n* and *m*, in $(ABO_3)_n/(AB'O_3)_m$ heterostructures. Two-dimensional Monte Carlo simulations of ordered $(LaFeO_3)_n/(LaCrO_3)_n$ lattices produced increasingly complex magnetic structures as the superlattice period was increased; $n = 2$ yielded an E-type AF structure, and $n = 4$ resulted in multiple ordering wave vectors (106). Experimental work proving the stability of these spin structures has not yet been reported and therefore represents unexplored territory in oxide

heterostructures. Additionally, although the measured magnetic and transport behavior in the (110)- and (001)-oriented $(ABO_3)_1/(AB'O_3)_1$ superlattices described above is consistent with AF order, neutron diffraction experiments proving the spin structure are yet to be reported.

3.4. Dimensionality and Magnetism in Superlattices

Even in the absence of charge transfer or significant *B*-O-*B′* exchange interactions, novel magnetic properties can arise in $(ABO_3)/(AB'O_3)$ superlattices due to two-dimensional confinement of carriers. Although this is a nascent field of study, recent measurements of magnetic behavior in $(LaNiO_3)_n/(LaAlO_3)_n$ superlattices provide an intriguing example. Bulk rare earth nickelates exhibit an insulating AF ground state, with the exception of $LaNiO_3$, which is paramagnetic and metallic. Although no evidence for magnetic ordering is observed in superlattices with $n = 3, 4$, muon spin rotation measurements of $n = 2$ superlattices indicate an AF state with $T_N = 50$ K (107). Subsequent resonant X-ray diffraction measurements of magnetic (1/4 1/4 *L*) reflections confirmed the presence of long-range ordering in $n = 2$ samples (108). Additionally, the azimuthal intensity dependence of this peak is indicative of a noncollinear magnetic structure, the spin orientation of which is coupled to the strain-induced orbital polarization. The general observation of magnetic ordering in $LaNiO_3$-based superlattices has catalyzed theoretical studies of magnetic phase stability in confined nickelates as a function of layer thickness and epitaxial strain (109–111).

3.5. Extrinsic Effects and Interfacial Magnetism: Vacancies, Stoichiometry, and Intermixing

Extrinsic effects such as oxygen vacancies, local nonstoichiometry, and cation intermixing are always present to some degree at real interfaces, and in some cases these effects dominate magnetic behavior. As magnetic ordering is often sensitively dependent on the nominal *B*-site valence state, the presence of oxygen vacancies and/or cation nonstoichiometry can induce magnetic behavior in films that is quite different from that of their bulk stoichiometric counterparts. An example is $LaMnO_3$, which has a strong propensity for cation vacancies. Although stoichiometric $LaMnO_3$ is an A-type antiferromagnet, cation nonstoichiometry decreases the Mn valence state, inducing FM behavior (112). Therefore, quantitative measurements of cation stoichiometry, for instance, with Rutherford backscattering spectroscopy, are a critical first step in identifying the origin of unexpected magnetic behavior in films. Oxygen vacancies, which can also modify magnetic behavior by altering the nominal *B*-site valence, present a more difficult challenge to an experimentalist, as there is no direct method by which to quantify oxygen stoichiometry in ultrathin films.

Although oxygen vacancies provide a means for reducing a *B*-site cation out of an unfavorable valence state (e.g., Fe^{4+}, Co^{4+}, Ni^{3+}), epitaxial strain can provide a further driving force for vacancy formation. Oxygen vacancies couple strongly to the lattice, inducing changes to the *B*-O bond lengths and unit cell volume. Thus, ordered planes of oxygen vacancies provide an avenue, in addition to octahedral distortions and rotations, for relieving the elastic energy incurred by strain. For example, in $La_{0.5}Sr_{0.5}CoO_{3-\delta}$ films, ordered oxygen vacancies are a mechanism for strain relaxation (113–115). The vacancies, which expand the Co-O bond lengths, order on (100) and (010) planes in films under tensile strain and on (001) planes in films under compressive strain. The relationship between strain and vacancy formation energy has also been investigated by using computational techniques (116–118). Density functional theory calculations of strained $CaMnO_3$ reveal a reduction of the formation energy for oxygen vacancies with increasing tensile strain and show that the energetically favorable vacancy ordering under tensile strain is on the (100) and

(010) planes (116). This coupling between the equilibrium vacancy concentration and epitaxial strain can complicate the physical interpretation of studies focused on strain-induced magnetic behavior in films containing magnetic cations in high oxidation states.

Compositional variations through the thickness of a film can also lead to variations in magnetic properties at surfaces and interfaces compared with magnetic properties in the noninterfacial region. These depth-dependent chemical changes can arise from cation segregation, as in $La_{1-x}Sr_xMnO_3$ and $La_{1-x}Ca_xMnO_3$ films, in which multiple groups have reported surface segregation of Sr and Ca (119–123). An additional mechanism for compositional gradients is vacancy accumulation near interfaces. For instance, an increased concentration of oxygen vacancies in the near-interfacial region of $La_{1-x}Sr_xCoO_{3-\delta}$ on $SrTiO_3$ has been observed with scanning transmission electron microscopy–electron energy loss spectroscopy (STEM-EELS), leading to magnetic phase separation in the cobaltite near the film/substrate interface (124). Evidence for the accumulation of oxygen vacancies has also been reported at LSMO/$SrRuO_3$ interfaces (125), a system of interest due to the novel interfacial magnetic coupling of Mn and Ru cations (126–128).

Finally, identifying the origin of interfacial magnetism requires a detailed understanding of cation intermixing at interfaces, which can be quantified by using techniques such as STEM-EELS, ion scattering, and X-ray scattering (123, 129–132). Multiple studies have revealed differences in the profiles of *A*-site and *B*-site diffusion across interfaces (130, 132–134). Additionally, intermixing and interfacial roughness can depend on the specifics of interfacial termination (135, 136), producing asymmetries in the behavior of *A*/*B* and *B*/*A* interfaces (29). These deviations from perfectly abrupt interfaces have important consequences for magnetization, as intermixing and roughness can change the local valence of the *B*-site cation and alter the average number of *B*-O-*B′* bonds at an interface. For example, density functional theory calculations of the BFO/LSMO interface found that AF coupling of the Mn-Fe spins is energetically favorable in the presence of intermixing but that, at abrupt interfaces, the formation of a net magnetization in BFO is not favorable (137). These issues highlight the need for extensive compositional and structural characterization, using local or depth-resolved probes, in combination with magnetic characterization to fully elucidate the origins of novel magnetic behavior at oxide interfaces.

4. CONCLUDING REMARKS AND FUTURE DIRECTIONS

We review the physical mechanisms that lead to novel magnetic behavior in perovskite oxide heterostructures and at heterointerfaces. By utilizing the GKA rules as a foundation for understanding exchange interactions in complex oxides, we provide basic principles and examples of how charge transfer, interfacial atomic structure, orbital reconstructions, and the number of interfacial *B*-O-*B′* bonds can alter magnetism at various length scales near an interface. With all these mechanisms available to influence interfacial magnetism, obtaining quantitative experimental measurements of *B*-O-*B* bond angles and lengths, charge transfer, orbital polarization, and magnetization at buried interfaces remains a key challenge. Advanced characterization techniques will play an increasingly critical role in disentangling the effects of local atomic structure and composition, orbital polarization, and charge transfer on interfacial magnetism. Recent demonstrations have shown the ability of STEM (78, 79, 86, 138) and synchrotron-based multiple Bragg rod analysis (123, 139–141) to resolve subtle changes in lattice distortions and composition as a function of distance from a heterointerface. The newly developed orbital reflectometry technique, which combines soft-X-ray reflectivity with linear dichroism, provides an avenue to depth-profile orbital polarization in heterostructures (142). Advances in hard-X-ray photoemission have enabled the study of electronic structure at buried heterojunctions (143, 144). We envision significant progress over the next decade in better understanding the physical origins of interfacial magnetism by combining these

structural/orbital/electronic probes with techniques capable of measuring and depth-resolving magnetism at interfaces, including XMCD and polarized neutron reflectometry. These magnetic probes are especially valuable as techniques complementary to conventional magnetometry methods, which can yield spurious results when applied to low-signal samples (145), such as a few magnetic unit cells at an interface.

Finally, we highlight some underexplored areas and emerging research directions that may enable new strategies for or insights into the design and control of magnetism in oxide heterostructures. The vast majority of work on oxide heterostructures has centered on *A/B* interfaces or superlattices; however, the synthesis techniques used in depositing these heterostructures are quite capable of producing more complex structures such as multicomponent superlattices. We believe that multicomponent heterostructures or superlattices with complex periodicities are an underexplored area with the potential for interesting magnetic behavior. An example is so-called tricolor superlattices, with three constituent materials forming an *ABC* periodicity, in which inversion symmetry is broken, enabling interesting magnetoelectric phenomena (146–148). The addition of a third component can also induce magnetic frustration through the creation of two interfaces (*A/B* and *B/C*) with distinct and possibly competing interactions (149). The use of external electric or magnetic fields to alter interfacial charge transfer and/or orbital reconstructions may also prove to be a fruitful area of research, in particular in moving the study of interfacial magnetism along a more applied path. At interfaces, the intrinsic electric field due to broken inversion symmetry and charge transfer and the effects of dimensional confinement can cause new magnetic states to emerge. Stabilizing spin spiral states via the Dzyaloshinskii-Moriya interaction may be possible (150). These states may in principle be tuned by gate electric fields via the Rashba effect.

DISCLOSURE STATEMENT

The authors are not aware of any affiliations, memberships, funding, or financial holdings that might be perceived as affecting the objectivity of this review.

ACKNOWLEDGMENTS

We thank James Rondinelli and Daniel Khomskii for helpful discussions. We acknowledge Eun Ju Moon for the graphics of 3*d* orbitals. S.J.M. acknowledges financial support from the Army Research Office (W911NF-12-1-0132) and from the Office of Naval Research (ONR N00014-11-1-0109). A.B. was supported by the Materials Science and Engineering Division, Basic Energy Sciences program, US Department of Energy, under contract number DE-AC02-06CH11357.

LITERATURE CITED

1. Goodenough JB. 1963. *Magnetism and the Chemical Bond*. New York: Interscience
2. Maekawa S. 2004. Introduction. In *Physics of Transition Metal Oxides*, ed. S Maekawa, T Tohyama, SE Barnes, S Ishihara, W Koshibae, G Khaliullin, pp. 1–35. Berlin: Springer
3. Hwang HY, Iwasa Y, Kawasaki M, Keimer B, Nagaosa N, Tokura Y. 2012. Emergent phenomena at oxide interfaces. *Nat. Mater.* 11:103–13
4. Fusil S, Garcia V, Barthélémy A, Bibes M. 2014. Magnetoelectric devices for spintronics. *Annu. Rev. Mater. Res.* 44:91–116
5. Ramesh R, Spaldin NA. 2007. Multiferroics: progress and prospects in thin films. *Nat. Mater.* 6:21–29
6. Bea H, Gajek M, Bibes M, Barthelemy A. 2008. Spintronics with multiferroics. *J. Phys. Condens. Matter* 20:434221

7. Goldschmidt VM. 1926. Die Gesetze der Krystallochemie. *Naturwissenschaften* 21:477–85
8. Glazer AM. 1972. Classification of tilted octahedra in perovskites. *Acta Crystallogr. B* 28:3384–92
9. Goodenough JB. 1955. Theory of the role of covalence in the perovskite-type manganites [La,*M*(II)]MnO_3. *Phys. Rev.* 100:564–73
10. Kanamori J. 1959. Superexchange interaction and symmetry properties of electron orbitals. *J. Phys. Chem. Solids* 10:87–98
11. Anderson PW. 1950. Antiferromagnetism. Theory of superexchange interaction. *Phys. Rev.* 79:350–56
12. Khomskii D. 2001. Electronic structure, exchange and magnetism in oxides. In *Spin Electronics*, ed. MJ Thornton, M Ziese, pp. 89–116. Berlin/Heidelberg, Ger.: Springer-Verlag
13. Stöhr J, Siegmann HC. 2006. *Magnetism: From Fundamentals to Nanoscale Dynamics*. Berlin/Heidelberg, Ger.: Springer-Verlag
14. Zaanen J, Sawatzky GA, Allen JW. 1985. Band gaps and electronic structure of transition-metal compounds. *Phys. Rev. Lett.* 55:418–21
15. Ushakov AV, Streltsov SV, Khomskii DI. 2011. Crystal field splitting in correlated systems with negative charge-transfer gap. *J. Phys. Condens. Matter* 23:445601
16. Zener C. 1951. Interactions between the *d*-shells in transition metals. II. Ferromagnetic compounds of manganese with perovskite structure. *Phys. Rev.* 82:403–5
17. Anderson PW, Hasegawa H. 1955. Considerations on double exchange. *Phys. Rev.* 100:675–81
18. de Gennes P-G. 1960. Effects of double exchange in magnetic crystals. *Phys. Rev.* 118:141–54
19. Ohtomo A, Hwang HY. 2004. A high-mobility electron gas at the $LaAlO_3/SrTiO_3$ heterointerface. *Nature* 427:423–26
20. Yunoki S, Moreo A, Dagotto E, Okamoto S, Kancharla SS, Fujimori A. 2007. Electron doping of cuprates via interfaces with manganites. *Phys. Rev. B* 76:064532
21. Ohtomo A, Muller DA, Grazul JL, Hwang HY. 2002. Artificial charge-modulation in atomic-scale perovskite titanate superlattices. *Nature* 419:378–80
22. Salvador PA, Haghiri-Gosnet A-M, Mercey B, Hervieu M, Raveau B. 1999. Growth and magnetoresistive properties of $(LaMnO_3)_m(SrMnO_3)_n$ superlattices. *Appl. Phys. Lett.* 75:2638–40
23. Verbeeck J, Lebedev OI, Van Tendeloo G, Mercey B. 2002. $SrTiO_3$ (100)/$(LaMnO_3)_m(SrMnO_3)_n$ layered heterostructures: a combined EELS and TEM study. *Phys. Rev. B* 66:184426
24. Okamoto S, Millis AJ. 2004. Electronic reconstruction at an interface between a Mott insulator and a band insulator. *Nature* 428:630–33
25. Lin C, Okamoto S, Millis AJ. 2006. Dynamical mean-field study of model double-exchange superlattices. *Phys. Rev. B* 73:041104(R)
26. Sawa A, Yamamoto A, Yamada H, Fujii T, Kawasaki M, et al. 2007. Fermi level shift in $La_{1-x}Sr_xMO_3$ (M = Mn, Fe, Co, and Ni) probed by Schottky-like heteroepitaxial junctions with $SrTi_{0.99}Nb_{0.01}O_3$. *Appl. Phys. Lett.* 90:252102
27. Nakamura M, Sawa A, Fujioka J, Kawasaki M, Tokura Y. 2010. Interface band profiles of Mott-insulator/Nb:$SrTiO_3$ heterojunctions as investigated by optical spectroscopy. *Phys. Rev. B* 82:201101(R)
28. Paulsen JM, Thomas CL, Dahn JR. 2000. O_2 structure $Li_{2/3}[Ni_{1/3}Mn_{2/3}]O_2$: a new layered cathode material for rechargeable lithium batteries. I. Electrochemical properties. *J. Electrochem. Soc.* 147:861–68
29. May SJ, Shah AB, te Velthuis SGE, Fitzsimmons MR, Zuo JM, et al. 2008. Magnetically asymmetric interfaces in a $LaMnO_3/SrMnO_3$ superlattice due to structural asymmetries. *Phys. Rev. B* 77:174409
30. Monkman EJ, Adamo C, Mundy JA, Shai DE, Harter JW, et al. 2012. Quantum many-body interactions in digital oxide superlattices. *Nat. Mater.* 11:855–59
31. Bhattacharya A, May SJ, te Velthuis SGE, Warusawithana M, Zhai X, et al. 2008. Metal-insulator transition and its relation to magnetic structure in $(LaMnO_3)_{2n}/(SrMnO_3)_n$ superlattices. *Phys. Rev. Lett.* 100:257203
32. Adamo C, Ke X, Schiffer P, Soukiassian A, Warusawithana M, et al. 2008. Electrical and magnetic properties of $(SrMnO_3)_n/(LaMnO_3)_{2n}$ superlattices. *Appl. Phys. Lett.* 92:112508
33. Perucchi A, Baldassarre L, Nucara A, Calvani P, Adamo C, et al. 2010. Optical properties of $(SrMnO_3)_n/(LaMnO_3)_{2n}$ superlattices: an insulator-to-metal transition observed in the absence of disorder. *Nano Lett.* 10:4819–23

34. Aruta C, Adamo C, Galdi A, Orgiani P, Bisogni V, et al. 2009. Evolution of magnetic phases and orbital occupation in $(SrMnO_3)_n/(LaMnO_3)_{2n}$ superlattices. *Phys. Rev. B* 80:140405(R)
35. May SJ, Ryan PJ, Robertson JL, Kim JW, Santos TS, et al. 2009. Enhanced ordering temperatures in antiferromagnetic manganite superlattices. *Nat. Mater.* 8:892–97
36. Hemberger J, Krimmel A, Kurz T, Krug von Nidda H-A, Ivanov VY, et al. 2002. Structural, magnetic, and electrical properties of single-crystalline $La_{1-x}Sr_xMnO_3$ ($0.4 < x < 0.85$). *Phys. Rev. B* 66:094410
37. Burgy J, Mayr M, Martin-Mayor V, Moreo A, Dagotto E. 2001. Colossal effects in transition metal oxides caused by intrinsic inhomogeneities. *Phys. Rev. Lett.* 87:277202
38. Kagan MY, Khomskii DI, Mostovoy MV. 1999. Double-exchange model: phase separation versus canted spins. *Eur. Phys. J. B* 12:217–23
39. Santos TS, May SJ, Robertson JL, Bhattacharya A. 2009. Tuning between the metallic antiferromagnetic and ferromagnetic phases of $La_{1-x}Sr_xMnO_3$ near $x = 0.5$ by digital synthesis. *Phys. Rev. B* 80:155114
40. Santos TS, Kirby BJ, Kumar S, May SJ, Borchers JA, et al. 2011. Delta doping of ferromagnetism in antiferromagnetic manganite superlattices. *Phys. Rev. Lett.* 107:167202
41. Ahn CH, Bhattacharya A, Di Ventra M, Eckstein JN, Frisbie CD, et al. 2006. Electrostatic modification of novel materials. *Rev. Mod. Phys.* 78:1185–212
42. Hong X, Posadas A, Lin A, Ahn CH. 2003. Ferroelectric-field-induced tuning of magnetism in the colossal magnetoresistive oxide $La_{1-x}Sr_xMnO_3$. *Phys. Rev. B* 68:134415
43. Dhoot AS, Israel C, Moya X, Mathur ND, Friend RH. 2009. Large electric field effect in electrolyte-gated manganites. *Phys. Rev. Lett.* 102:136402
44. Vaz CAF, Hoffman J, Segal Y, Reiner JW, Grober RD, et al. 2010. Origin of the magnetoelectric coupling effect in $Pb(Zr_{0.2}Ti_{0.8})O_3/La_{0.8}Sr_{0.2}MnO_3$ multiferroic heterostructures. *Phys. Rev. Lett.* 104:127202
45. Burton JD, Tsymbal EY. 2009. Prediction of electrically induced magnetic reconstruction at the manganite/ferroelectric interface. *Phys. Rev. B* 80:174406
46. Radaelli PG, Iannone G, Marezio M, Hwang HY, Cheong SW, et al. 1997. Structural effects on the magnetic and transport properties of perovskite $A_{1-x}A_x'MnO_3$ ($x = 0.25, 0.30$). *Phys. Rev. B* 56:8265–76
47. Subramanian MA, Ramirez AP, Marshall WJ. 1999. Structural tuning of ferromagnetism in a 3D cuprate perovskite. *Phys. Rev. Lett.* 82:1558–61
48. Gorbenko OY, Samoilenkov SV, Graboy IE, Kaul AR. 2002. Epitaxial stabilization of oxides in thin films. *Chem. Mater.* 14:4026–43
49. Yakel HL, Koehler WC, Bertaut EF, Forrat EF. 1963. On the crystal structure of the manganese (III) trioxides of the heavy lanthanides and yttrium. *Acta Crystallogr.* 16:957–62
50. Graboy IE, Bosak AA, Gorbenko OY, Kaul AR, Dubourdieu C, et al. 2003. HREM study of epitaxially stabilized hexagonal rare earth manganites. *Chem. Mater.* 15:2632–37
51. Balasubramaniam KR, Havelia S, Salvador PA, Zheng H, Mitchell JF. 2007. Epitaxial stabilization and structural properties of $REMnO_3$ (RE = Dy,Gd,Sm) compounds in a layered, hexagonal ABO_3 structure. *Appl. Phys. Lett.* 91:232901
52. Wadati H, Okamoto J, Garganourakis M, Scagnoli V, Staub U, et al. 2012. Origin of the large polarization in multiferroic $YMnO_3$ thin films revealed by soft- and hard-X-ray diffraction. *Phys. Rev. Lett.* 108:047203
53. Marti X, Skumryev V, Laukhin V, Bachelet R, Ferrater C, et al. 2010. Strain-driven noncollinear magnetic ordering in orthorhombic epitaxial $YMnO_3$ thin films. *J. Appl. Phys.* 108:123917
54. Fina I, Fabrega L, Marti X, Sanchez F, Fontcuberta J. 2011. Chiral domains in cycloidal multiferroic thin films: switching and memory effects. *Phys. Rev. Lett.* 107:257601
55. Kozuka Y, Seki H, Fujita TC, Chakraverty S, Yoshimatsu K, et al. 2012. Epitaxially stabilized $EuMoO_3$: a new itinerant ferromagnet. *Chem. Mater.* 24:3746–50
56. Rondinelli JM, May SJ, Freeland JW. 2012. Control of octahedral connectivity in perovskite oxide heterostructures: an emerging route to multifunctional materials discovery. *MRS Bull.* 37:261–70
57. Tomioka Y, Tokura Y. 2004. Global phase diagram of perovskite manganites in the plane of quenched disorder versus one-electron bandwidth. *Phys. Rev. B* 70:014432
58. Millis AJ, Darling T, Migliori A. 1998. Quantifying strain dependence in "colossal" magnetoresistance manganites. *J. Appl. Phys.* 83:1588–91
59. Konishi Y, Fang Z, Izumi M, Manako T, Kasai M, et al. 1999. Orbital-state-mediated phase-control of manganites. *J. Phys. Soc. Jpn.* 68:3790–93

60. Fang Z, Solovyev IV, Terakura K. 2000. Phase diagram of tetragonal manganites. *Phys. Rev. Lett.* 84:3169–72
61. Baena A, Brey L, Calderón MJ. 2011. Effect of strain on the orbital and magnetic ordering of manganite thin films and their interface with an insulator. *Phys. Rev. B* 83:064424
62. Mukherjee A, Cole WS, Woodward P, Randeria M, Trivedi N. 2013. Theory of strain-controlled magnetotransport and stabilization of the ferromagnetic insulating phase in manganite thin films. *Phys. Rev. Lett.* 110:157201
63. Aruta C, Ghiringhelli G, Tebano A, Boggio NG, Brookes NB, et al. 2006. Strain induced X-ray absorption linear dichroism in $La_{0.7}Sr_{0.3}MnO_3$ thin films. *Phys. Rev. B* 73:235121
64. Adamo C, Ke X, Wang HQ, Xin HL, Heeg T, et al. 2009. Effect of biaxial strain on the electrical and magnetic properties of (001) $La_{0.7}Sr_{0.3}MnO_3$ thin films. *Appl. Phys. Lett.* 95:112504
65. Thiele C, Dorr K, Bilani O, Rodel J, Schultz L. 2007. Influence of strain on the magnetization and magnetoelectric effect in $La_{0.7}A_{0.3}MnO_3$/PMN-PT(001) (A = Sr,Ca). *Phys. Rev. B* 75:054408
66. Boschker H, Mathews M, Houwman EP, Nishikawa H, Vailionis A, et al. 2009. Strong uniaxial in-plane magnetic anisotropy of (001)- and (011)-oriented $La_{0.67}Sr_{0.33}MnO_3$ thin films on $NdGaO_3$ substrates. *Phys. Rev. B* 79:214425
67. Demidov VV, Ovsyannikov GA, Petrzhik AM, Borisenko IV, Shadrin AV, Gunnarsson R. 2013. Magnetic anisotropy in strained manganite films and bicrystal junctions. *J. Appl. Phys.* 113:163909
68. Lee JH, Fang L, Vlahos E, Ke XL, Jung YW, et al. 2010. A strong ferroelectric ferromagnet created by means of spin-lattice coupling. *Nature* 466:954–58
69. Fennie CJ, Rabe KM. 2006. Magnetic and electric phase control in epitaxial $EuTiO_3$ from first principles. *Phys. Rev. Lett.* 97:267602
70. Fuchs D, Arac E, Pinta C, Schuppler S, Schneider R, Lohneysen Hv. 2008. Tuning the magnetic properties of $LaCoO_3$ thin films by epitaxial strain. *Phys. Rev. B* 77:014434
71. Freeland JW, Ma JX, Shi J. 2008. Ferromagnetic spin-correlations in strained $LaCoO_3$ thin films. *Appl. Phys. Lett.* 93:212501
72. Mehta VV, Liberati M, Wong FJ, Chopdekar RV, Arenholz E, Suzuki Y. 2009. Ferromagnetism in tetragonally distorted $LaCoO_3$ thin films. *J. Appl. Phys.* 105:07E503
73. Pinta C, Fuchs D, Merz M, Wissinger M, Arac E, et al. 2008. Suppression of spin-state transition in epitaxially strained $LaCoO_3$. *Phys. Rev. B* 78:174402
74. Klie RF, Yuan T, Tanase M, Yang G, Ramasse Q. 2010. Direct measurement of ferromagnetic ordering in biaxially strained $LaCoO_3$ thin films. *Appl. Phys. Lett.* 96:082510
75. Hsu H, Blaha P, Wentzcovitch RM. 2012. Ferromagnetic insulating state in tensile-strained $LaCoO_3$ thin films from LDA+U calculations. *Phys. Rev. B* 85:140404(R)
76. Seo H, Posadas A, Demkov AA. 2012. Strain-driven spin-state transition and superexchange interaction in $LaCoO_3$: ab initio study. *Phys. Rev. B* 86:014430
77. Fujioka J, Yamasaki Y, Nakao H, Kumai R, Murakami Y, et al. 2013. Spin-orbital superstructure in strained ferrimagnetic perovskite cobalt oxide. *Phys. Rev. Lett.* 111:027206
78. Jia CL, Mi SB, Faley M, Poppe U, Schubert J, Urban K. 2009. Oxygen octahedron reconstruction in the $SrTiO_3/LaAlO_3$ heterointerfaces investigated using aberration-corrected ultrahigh-resolution transmission electron microscopy. *Phys. Rev. B* 79:081405(R)
79. Borisevich AY, Chang HJ, Huijben M, Oxley MP, Okamoto S, et al. 2010. Suppression of octahedral tilts and associated changes in electronic properties at epitaxial oxide heterostructure interfaces. *Phys. Rev. Lett.* 105:087204
80. May SJ, Smith CR, Kim JW, Karapetrova E, Bhattacharya A, Ryan PJ. 2011. Control of octahedral rotations in $(LaNiO_3)_n/(SrMnO_3)_m$ superlattices. *Phys. Rev. B* 83:153411
81. Zhang JY, Hwang J, Raghavan S, Stemmer S. 2013. Symmetry lowering in extreme-electron-density perovskite quantum wells. *Phys. Rev. Lett.* 110:256401
82. Rondinelli JM, Spaldin NA. 2010. Substrate coherency driven octahedral rotations in perovskite oxide films. *Phys. Rev. B* 82:113402
83. He J, Borisevich A, Kalinin SV, Pennycook SJ, Pantelides ST. 2010. Control of octahedral tilts and magnetic properties of perovskite oxide heterostructures by substrate symmetry. *Phys. Rev. Lett.* 105:227203

84. Aso R, Kan D, Shimakawa Y, Kurata H. 2013. Atomic level observation of octahedral distortions at the perovskite oxide heterointerface. *Sci. Rep.* 3:2214
85. Petrov AY, Torrelles X, Verna A, Xu H, Cossaro A, et al. 2013. Surface octahedral distortions and atomic design of perovskite interfaces. *Adv. Mater.* 25:4043–38
86. Zhang JY, Jackson CA, Raghavan S, Hwang J, Stemmer S. 2013. Magnetism and local structure in low-dimensional Mott insulating $GdTiO_3$. *Phys. Rev. B* 88:121104(R)
87. Hwang J, Zhang JY, Son J, Stemmer S. 2012. Nanoscale quantification of octahedral tilts in perovskite films. *Appl. Phys. Lett.* 100:191909
88. Komarek AC, Roth H, Cwik M, Stein WD, Baier J, et al. 2007. Magnetoelastic coupling in $RTiO_3$ (R = La,Nd,Sm,Gd,Y) investigated with diffraction techniques and thermal expansion measurements. *Phys. Rev. B* 75:224402
89. Chakhalian J, Freeland JW, Habermeier H-U, Cristiani G, Khaliullin G, et al. 2007. Orbital reconstruction and covalent bonding at an oxide interface. *Science* 318:1114–17
90. Yu P, Lee JS, Okamoto S, Rossell MD, Huijben M, et al. 2010. Interface ferromagnetism and orbital reconstruction in $BiFeO_3$-$La_{0.7}Sr_{0.3}MnO_3$ heterostructures. *Phys. Rev. Lett.* 105:027201
91. Calderón MJ, Liang S, Yu R, Salafranca J, Dong S, et al. 2011. Magnetoelectric coupling at the interface of $BiFeO_3/La_{0.7}Sr_{0.3}MnO_3$ multilayers. *Phys. Rev. B* 84:024422
92. Chakhalian J, Freeland JW, Srajer G, Strempfer J, Khaliullin G, et al. 2006. Magnetism at the interface between ferromagnetic and superconducting oxides. *Nat. Phys.* 2:244–48
93. Ueda K, Tabata H, Kawai T. 1998. Ferromagnetism in $LaFeO_3$-$LaCrO_3$ superlattices. *Science* 280:1064–66
94. Ueda K, Tabata H, Kawai T. 2001. Control of magnetic properties in $LaCrO_3$-$LaFeO_3$ artificial superlattices. *J. Appl. Phys.* 89:2847–51
95. Pickett WE. 1998. Spin-density-functional-based search for half-metallic antiferromagnets. *Phys. Rev. B* 57:10613–19
96. Miura K, Terakura K. 2001. Electronic and magnetic properties of La_2FeCrO_6: superexchange interaction for a d^5–d^3 system. *Phys. Rev. B* 63:104402
97. Ichikawa N, Arai M, Imai Y, Hagiwara K, Sakama H, et al. 2008. Multiferroism at room temperature in $BiFeO_3/BiCrO_3$ (111) artificial superlattices. *Appl. Phys. Express* 1:101302
98. Chakraverty S, Ohtomo A, Okuyama D, Saito M, Okude M, et al. 2011. Ferrimagnetism and spontaneous ordering of transition metals in double perovskite La_2CrFeO_6 films. *Phys. Rev. B* 84:064436
99. Tanaka H, Kawai T. 2000. Effect of magnetic exchange interactions in $La(Sr)MnO_3/LaMO_3$ (M = Fe, Cr, Co, Ni) artificial superlattices and their magnetic/electrical properties. *J. Appl. Phys.* 88:1559–65
100. Gibert M, Zubko P, Scherwitzl R, Iniguez J, Triscone JM. 2012. Exchange bias in $LaNiO_3$-$LaMnO_3$ superlattices. *Nat. Mater.* 11:195–98
101. Dong S, Dagotto E. 2013. Quantum confinement induced magnetism in $LaNiO_3$-$LaMnO_3$ superlattices. *Phys. Rev. B* 87:195116
102. Hoffman J, Tung IC, Nelson-Cheeseman BB, Liu M, Freeland JW, Bhattacharya A. 2013. Charge transfer and interfacial magnetism in $(LaNiO_3)_n/(LaMnO_3)_2$ superlattices. *Phys. Rev. B* 88:144411
103. Ueda K, Tabata H, Kawai T. 1999. Atomic arrangement and magnetic properties of $LaFeO_3$-$LaMnO_3$ artificial superlattices. *Phys. Rev. B* 60:R12561–64
104. Takamura Y, Yang F, Kemik N, Arenholz E, Biegalski MD, Christen HM. 2009. Competing interactions in ferromagnetic/antiferromagnetic perovskite superlattices. *Phys. Rev. B* 80:180417(R)
105. Chen YB, Zhou J, Zhang ST, Wu FX, Yao SH, et al. 2013. Significant ferrimagnetisms observed in superlattice composed of antiferromagnetic $LaFeO_3$ and $YMnO_3$. *Appl. Phys. Lett.* 102:042403
106. Zhu YY, Dong S, Zhang QF, Yunoki S, Wang YG, Liu JM. 2011. Tailoring magnetic orders in $(LaFeO_3)_n$-$(LaCrO_3)_n$ superlattices model. *J. Appl. Phys.* 110:053916
107. Boris AV, Matiks Y, Benckiser E, Frano A, Popovich P, et al. 2011. Dimensionality control of electronic phase transitions in nickel-oxide superlattices. *Science* 332:937–40
108. Frano A, Schierle E, Haverkort MW, Lu Y, Wu M, et al. 2013. Orbital control of noncollinear magnetic order in nickel oxide heterostructures. *Phys. Rev. Lett.* 111:106804
109. Lee SB, Chen R, Balents L. 2011. Metal-insulator transition in a two-band model for the perovskite nickelates. *Phys. Rev. B* 84:165119

110. Puggioni D, Filippetti A, Fiorentini V. 2012. Ordering and multiple phase transitions in ultrathin nickelate superlattices. *Phys. Rev. B* 86:195132
111. Lau B, Millis AJ. 2013. Theory of the magnetic and metal-insulator transitions in RNiO$_3$ bulk and layered structures. *Phys. Rev. Lett.* 110:126404
112. Topfer J, Goodenough JB. 1997. LaMnO$_{3+d}$ revisited. *J. Solid State Chem.* 130:117–28
113. Gazquez J, Bose S, Sharma M, Torija MA, Pennycook SJ, et al. 2013. Lattice mismatch accommodation via oxygen vacancy ordering in epitaxial La$_{0.5}$Sr$_{0.5}$CoO$_{3-\delta}$ thin films. *APL Mater.* 1:012105
114. Klenov DO, Donner W, Foran B, Stemmer S. 2003. Impact of stress on oxygen vacancy ordering in epitaxial (La$_{0.5}$Sr$_{0.5}$)CoO$_{3-\delta}$ thin films. *Appl. Phys. Lett.* 82:3427–29
115. Donner W, Chen CL, Liu M, Jacobson AJ, Lee Y-L, et al. 2011. Epitaxial strain–induced chemical ordering in La$_{0.5}$Sr$_{0.5}$CoO$_{3-\delta}$ films on SrTiO$_3$. *Chem. Mater.* 23:984–88
116. Aschauer U, Pfenninger R, Selbach SM, Grande T, Spaldin NA. 2013. Strain-controlled oxygen vacancy formation and ordering in CaMnO$_3$. *Phys. Rev. B* 88:054111
117. Chen X-Y, Chen L-J, Yang X-B, Zhao Y-J, Ding H-C, Duan C-G. 2012. Tuning the polarization and magnetism in BiCoO$_3$ by strain and oxygen vacancy effect: a first-principle study. *J. Appl. Phys.* 111:013901
118. Yang Q, Cao JX, Ma Y, Zhou YC, Jiang LM, Zhong XL. 2013. Strain effects on formation and migration energies of oxygen vacancy in perovskite ferroelectrics: a first-principles study. *J. Appl. Phys.* 113:184110
119. Bertacco R, Contour JP, Barthelemy A, Olivier J. 2002. Evidence for strontium segregation in La$_{0.7}$Sr$_{0.3}$MnO$_3$ thin films grown by pulsed laser deposition: consequences for tunnelling junctions. *Surf. Sci.* 511:366–72
120. Fister TT, Fong DD, Eastman JA, Baldo PM, Highland MJ, et al. 2008. In situ characterization of strontium surface segregation in epitaxial La$_{0.7}$Sr$_{0.3}$MnO$_3$ thin films as a function of oxygen partial pressure. *Appl. Phys. Lett.* 93:151904
121. Estrade S, Rebled JM, Arbiol J, Peiro F, Infante IC, et al. 2009. Effects of thickness on the cation segregation in epitaxial (001) and (110) La$_{2/3}$Ca$_{1/3}$MnO$_3$ thin films. *Appl. Phys. Lett.* 95:072507
122. Li ZP, Bosman M, Yang Z, Ren P, Wang L, et al. 2012. Interface and surface cation stoichiometry modified by oxygen vacancies in epitaxial manganite films. *Adv. Funct. Mater.* 22:4312–21
123. Herger R, Willmott PR, Schleputz CM, Bjorck M, Pauli SA, et al. 2008. Structure determination of monolayer-by-monolayer grown La$_{1-x}$Sr$_x$MnO$_3$ thin films and the onset of magnetoresistance. *Phys. Rev. B* 77:085401
124. Torija MA, Sharma M, Gazquez J, Varela M, He CY, et al. 2011. Chemically driven nanoscopic magnetic phase separation at the SrTiO$_3$(001)/La$_{1-x}$Sr$_x$CoO$_3$ interface. *Adv. Mater.* 23:2711–15
125. Borisevich AY, Lupini AR, He J, Eliseev EA, Morozovska AN, et al. 2012. Interface dipole between two metallic oxides caused by localized oxygen vacancies. *Phys. Rev. B* 86:140102(R)
126. Ziese M, Vrejoiu I, Pippel E, Esquinazi P, Hesse D, et al. 2010. Tailoring magnetic interlayer coupling in La$_{0.7}$Sr$_{0.3}$MnO$_3$/SrRuO$_3$ superlattices. *Phys. Rev. Lett.* 104:167203
127. Solignac A, Guerrero R, Gogol P, Maroutian T, Ott F, et al. 2012. Dual antiferromagnetic coupling at La$_{0.67}$Sr$_{0.33}$MnO$_3$/SrRuO$_3$ interfaces. *Phys. Rev. Lett.* 109:027201
128. Ke X, Belenky LJ, Lauter V, Ambaye H, Bark CW, et al. 2013. Spin structure in an interfacially coupled epitaxial ferromagnetic oxide heterostructure. *Phys. Rev. Lett.* 110:237201
129. Chambers SA, Engelhard MH, Shutthanandan V, Zhu Z, Droubay TC, et al. 2010. Instability, intermixing and electronic structure at the epitaxial LaAlO$_3$/SrTiO$_3$(001) heterojunction. *Surf. Sci. Rep.* 65:317–52
130. Willmott PR, Pauli SA, Herger R, Schleputz CM, Martoccia D, et al. 2007. Structural basis for the conducting interface between LaAlO$_3$ and SrTiO$_3$. *Phys. Rev. Lett.* 99:155502
131. Kalabukhov AS, Boikov YA, Serenkov IT, Sakharov VI, Popok VN, et al. 2009. Cationic disorder and phase segregation in LaAlO$_3$/SrTiO$_3$ heterointerfaces evidenced by medium-energy ion spectroscopy. *Phys. Rev. Lett.* 103:146101
132. Colby R, Qiao L, Zhang KHL, Shutthanandan V, Ciston J, et al. 2013. Cation intermixing and electronic deviations at the insulating LaCrO$_3$/SrTiO$_3$(001) interface. *Phys. Rev. B* 88:155325
133. Muller DA, Kourkoutis LF, Murfitt M, Song JH, Hwang HY, et al. 2008. Atomic-scale chemical imaging of composition and bonding by aberration-corrected microscopy. *Science* 319:1073–76

134. Hillebrand R, Pippel E, Hesse D, Vrejoiu I. 2011. A study of intermixing in perovskite superlattices by simulation-supported c_s-corrected HAADF-STEM. *Phys. Status Solid. A* 208:2144–49
135. Nakagawa N, Hwang HY, Muller DA. 2006. Why some interfaces cannot be sharp. *Nat. Mater.* 5:204–9
136. Kourkoutis LF, Muller DA, Hotta Y, Hwang HY. 2007. Asymmetric interface profiles in $LaVO_3/SrTiO_3$ heterostructures grown by pulsed laser deposition. *Appl. Phys. Lett.* 91:163101
137. Neumann RF, Bahiana M, Binggeli N. 2012. Magnetic properties of $La_{0.67}Sr_{0.33}MnO_3/BiFeO_3(001)$ heterojunctions: chemically abrupt vs. atomic intermixed interface. *EPL* 100:67002
138. Varela M, Gazquez J, Pennycook SJ. 2012. STEM-EELS imaging of complex oxides and interfaces. *MRS Bull.* 37:29–35
139. Fong DD, Cionca C, Yacoby Y, Stephenson GB, Eastman JA, et al. 2005. Direct structural determination in ultrathin ferroelectric films by analysis of synchrotron X-ray scattering measurements. *Phys. Rev. B* 71:144112
140. Pauli SA, Leake SJ, Delley B, Bjorck M, Schneider CW, et al. 2011. Evolution of the interfacial structure of $LaAlO_3$ on $SrTiO_3$. *Phys. Rev. Lett.* 106:036101
141. Yamamoto R, Bell C, Hikita Y, Hwang HY, Nakamura H, et al. 2011. Structural comparison of *n*-type and *p*-type $LaAlO_3/SrTiO_3$ interfaces. *Phys. Rev. Lett.* 107:036104
142. Benckiser E, Haverkort MW, Bruck S, Goering E, Macke S, et al. 2011. Orbital reflectometry of oxide heterostructures. *Nat. Mater.* 10:189–93
143. Wadati H, Hotta Y, Fujimori A, Susaki T, Hwang HY, et al. 2008. Hard X-ray photoemission study of $LaAlO_3/LaVO_3$ multilayers. *Phys. Rev. B* 77:045122
144. Gray AX, Janotti A, Son J, LeBeau JM, Ueda S, et al. 2011. Insulating state of ultrathin epitaxial $LaNiO_3$ thin films detected by hard X-ray photoemission. *Phys. Rev. B* 84:075104
145. Garcia MA, Fernandez Pinel E, de la Venta J, Quesada A, Bouzas V, et al. 2009. Sources of experimental errors in the observation of nanoscale magnetism. *J. Appl. Phys.* 105:013925
146. Ogawa Y, Yamada H, Ogasawara T, Arima T, Okamoto H, et al. 2003. Nonlinear magneto-optical Kerr rotation of an oxide superlattice with artificially broken symmetry. *Phys. Rev. Lett.* 90:217403
147. Kida N, Yamada H, Sato H, Arima T, Kawasaki M, et al. 2007. Optical magnetoelectric effect of patterned oxide superlattices with ferromagnetic interfaces. *Phys. Rev. Lett.* 99:197404
148. Hatt AJ, Spaldin NA. 2007. Trilayer superlattices: a route to magnetoelectric multiferroics? *Appl. Phys. Lett.* 90:242916
149. Seo J, Phan BT, Stahn J, Lee J, Panagopoulos C. 2010. Relaxor characteristics at the interfaces of $NdMnO_3/SrMnO_3/LaMnO_3$ superlattices. *Phys. Rev. B* 82:140405(R)
150. Banerjee S, Erten O, Randeria M. 2013. Ferromagnetic exchange, spin-orbit coupling and spiral magnetism at the $LaAlO_3/SrTiO_3$ interface. *Nat. Phys.* 9:626–30